Research Square

Preprints are preliminary reports that have not undergone peer review.
They should not be considered conclusive, used to inform clinical practice,
or referenced by the media as validated information.

Explainable GNN Framework Guided by Local Chemical Features to Predict Binding Energies in Bimetallic Alloys

A. F. Usuga
Universitat Autònoma de Barcelona
C. S. Praveen
Cochin University of Science and Technology
A. Comas-Vives
aleix.comas@tuwien.ac.at
TU Wien

Article

Keywords:

Posted Date: September 23rd, 2025

DOI: https://doi.org/10.21203/rs.3.rs-7566600/v1

License: This work is licensed under a Creative Commons Attribution 4.0 International License. Read Full License

Additional Declarations: No competing interests reported.

Version of Record: A version of this preprint was published at npj Computational Materials on April 16th, 2026. See the published version at https://doi.org/10.1038/s41524-026-02045-6.

Abstract

Adsorption energies are key catalytic descriptors that reveal adsorbate-site interactions on heterogeneous catalysts. However, their computation via DFT is time-consuming, limiting high-throughput screening. This work presents a machine learning (ML) methodology based on graph representations of local adsorption sites, using a Graph Neural Network (GNN) with per-atom local descriptors derived from accessible physicochemical properties. The approach is evaluated on two bimetallic datasets. The first includes AB-type bimetallic flat surfaces with varying A:B ratios, predicting binding energies for small monodentate adsorbates (C, N, O, S, H) with MSEs of 0.073/0.181 eV (train/test). The second dataset comprises reaction energies of key intermediates for CO_2 hydrogenation on Ni-Ga-based surfaces. The GNN model achieves an impressive performance (MSE: 0.001/0.002 (train/test) eV) on complex atomic configurations, even bidentate ones. Beyond predictive performance, clustering analysis provides an explainable framework, showing how structural and electronic descriptors can rationally guide catalyst design and deepen understanding of adsorbate-metal interactions.

INTRODUCTION

Bimetallic alloys exhibit promising synergistic catalytic effects arising from interactions between their constituent atoms[1], often allowing them to overcome the catalytic limitations of their respective pure metals[2]. Beyond composition, factors such as morphology and surface structure also play a critical role in determining catalytic performance[3]. Accelerated screening methodologies are essential to correlate and rationalize the catalytic activity at the atomic level via structural, geometric, and electronic properties[4] of the catalysts' active sites. Accurate modeling of catalyst activity requires precise kinetic and thermodynamic calculations of adsorbate-metal interactions. As a starting point, thermodynamic evaluation of these interactions provides valuable insights into reaction mechanisms, helping to identify strategies for controlling side reactions and improving catalyst design[5,6]. In this context, binding energy calculations performed within the Density Functional Theory (DFT) framework are a key tool for evaluating the activity of bimetallic catalysts. However, the high computational cost of DFT simulations limits the exploration of the vast chemical compound space. To reduce the computational cost of DFT, approaches that use correlations such as scaling relations[7–11] and catalytic descriptors, like the *d*-band center,[12,13] have been proposed. Although these methods are intuitive and useful, they are relatively simple and fail to address some critical aspects of the interaction. This limitation is even more significant for bimetallic alloys, often resulting in poorly correlated models[11]. However, a promising approach has emerged to accelerate adsorption energy prediction: training machine learning (ML)

models using DFT-derived data[14,15]. These models predict bonding strength and help identify adsorption trends, providing valuable insights into catalytic behavior[16–19].

Several adsorption energy prediction models have traditionally relied on features defined in Euclidean space[20–22], using machine learning architectures such as Linear Regression, Gradient Boosting machines, Support Vector Machines, and Gaussian Process Regressors[23–26]. However, using Euclidean space, inputs force the adsorbate-metal interaction to be modelled with predefined feature representations, which restricts and oversimplifies the complexity of these interactions. This constraint limits capturing the complex nature of the catalytic surfaces, where atomic interactions depend on both local geometry and electronic effects. More adaptable and flexible ML-based architectures are required to accurately represent complex chemical interactions to overcome the limitations of traditional ML architectures[27,28]. One such approach that has gained significant attention is using Graph Neural Networks (GNNs). GNN-based architectures use graphs as inputs, which belong to non-Euclidean spaces. The graph represents the connectivity, and optionally the spatial relationship, between nodes, i.e., encoding chemical bond information, while nodes symbolize the atomic centers. This makes graphs a natural and intuitive way for capturing bonding interactions and chemical structures for molecular and catalytic systems. Evaluating the capabilities of GNN-based methodologies, early implementations focused on capturing chemical information for molecular systems[29–31]. For instance, using geometrical descriptors, such as bond distances and angles, the local reactivity of organic molecules with different functional groups was compared, with nodes including features that distinguish between atoms[32]. Since then, GNNs have been successfully applied in various impactful tasks[33], including material classification[34,35], and predicting molecular and solid-state properties[36–40].

Focusing on methodologies for predicting binding energies on metallic catalysts, two types of descriptors can be considered when using graph-based representations as input: edge and node attributes. Edge attributes typically encode bond distances, bond types, and other relevant geometric information, while node features define atom types. Among the frameworks employing edge descriptors, Crystal Graph Convolutional Neural Networks (CGCNNs) have become one of the most widely used architectures[41–45]. In CGCNN, bond distances and tabulated atomic properties are encoded as input features. This methodology is distinguished by its interpretability, offering insights into how each metal locally affects the adsorbate-metal interaction. CGCNNs have been successfully applied to various materials, including nanoparticles, 2D systems, and periodic surfaces. Other models requiring bond information as input include ACE-GCN[46], ALIGNN[47], GAT[48–50], all based on Graph Neural Networks (GNNs). These frameworks use graph convolutional-like operators to embed features by aggregating and transforming information from

neighboring nodes. An alternative approach involves Machine Learning Potentials (MLPs) using graph architectures[51–53]. MLPs go beyond simple atomic tabulated features, incorporating more complex descriptors such as SOAP (Smooth Overlap of Atomic Positions)[54]. Nevertheless, larger datasets are generally required than in previous architectures.

By employing edge attributes, models achieved high accuracy; however, their dependence on distance information does not alleviate the computational cost of DFT, as optimized adsorbate structures on the catalyst are still required. One alternative is using machine learning potentials (MLPs), but training such models demands extensive calculations and an exhaustive exploration of the potential energy surface (PES). Given this context, a promising solution is to employ GNN frameworks that rely only on node attributes. For instance, Pablo-García et al. [55] proposed a methodology that uses only one-hot encoding representation of the chemical element and the connectivity matrix to predict binding energies for large organic molecules. Their findings demonstrated that distinguishing atom types through a graph-based architecture can effectively model stable adsorbate structures. Building on this methodology, the impact of how neighboring nodes are defined has also been explored[56], which is a fundamental consideration when modeling complex adsorbate-metal interactions, particularly in cases where multidentate binding occurs[57]. Besides the advantage of using GNNs, it is essential to consider how the findings align with physicochemical insights and how the predictions regarding electronic and structural properties can be interpreted[58–62].

Aimed at developing a methodology that combines high predictive accuracy with improved interpretability in relating the catalyst's structure to its properties, our work presents a method for constructing a GNN-based model to predict binding/adsorption and reaction energies of complex species on bimetallic alloys. The methodology uses easily accessible atomic features as node attributes. Additionally, we demonstrate how one can directly predict these target quantities using features/properties only from the clean surface and the gas-phase adsorbate. To simplify the construction of the GNN-based model, only atomic connectivity is considered, preventing the need for bonding distances (edge attributes) as input in the graph representation. The selected inputs are designed to facilitate the structural analysis of each atom's impact on bonding interactions, identifying factors that influence bonding strength. The model's architecture was evaluated on two datasets. The first dataset consisted of monodentate adsorbates on flat facets, where the binding/adsorption energy is predicted. This dataset is constituted by A_nB_m alloys with systematic variation in their stoichiometry ratio, allowing the bonding interaction to be correlated at the atomic level with the catalyst's electronic structure. The second dataset contains Ni-Ga alloys, including systems such as Ni, Ni_3Ga, and Ni_5Ga_3, and includes both flat and stepped facets. Here, reaction energies for key intermediates in CO_2

hydrogenation to methanol are predicted. These Ni-based systems are interesting because Ni_3Ga has been computationally proposed as a promising, highly active catalyst for methanol, while experimental studies have shown that Ni_5Ga_3 performs better[63–65]. Therefore, understanding the structural origin of this catalytic performance is critical, and a localized description of the metallic adsorption site can provide valuable insights into how electronic and geometric factors influence interaction with key intermediates in CO_2 hydrogenation. This dataset also considers the effects of bidentate adsorbates and reaction energies influenced by multiple adsorbates. Finally, we assess the practicality and flexibility of using a GNN-based predictive model, highlighting its advantages over classical ML architectures.

RESULTS

Databases

In this work, two databases were used. The first database comes from a previously reported dataset of bimetallic alloys, which includes only monodentate adsorbates[66]. This dataset was chosen because we previously developed ML-based models using Gradient Boosting on Decision Trees, such as CatBoost[67] and XGBoost[68], classical ML architectures with input in Euclidean space, i.e., the inputs were numerical arrays with fixed shape[69]. Using this dataset, we aim to compare the strengths, limitations, and advantages of Euclidean-space-based methodologies with the non-Euclidean-space approach explored in this study, using graphs to represent the local adsorption sites.

The reported dataset for A_nB_m bimetallic alloys includes the relaxed structures on the clean surface, the adsorbate on the surface, and their total electronic energies. The alloy's surfaces expose flat (111) and (101) facets, with an FCC Bravais lattice. The stoichiometric composition of the modeled systems varies between the two elements at ratios of 0%, 25%, 50%, and 75%. In the A_nB_m bimetallic alloys, element A includes Ag, Au, Cu, Fe, Pt, and Zn, while element B encompasses all metals from groups 3 to 15 and periods IV to VI, including Al. The dataset contains monodentate adsorbates such as C, CH, CH_2, CH_3, H, N, NH, O, OH, H_2O, S, and SH, resulting in 17,343 data points. These adsorbates can be bound at the top, bridge, or hollow sites. As in our previously reported model, this study only extracts the relaxed geometries of the clean surfaces, with additional DFT calculations performed to generate descriptors for both the clean metallic surfaces and the free adsorbates in the gas phase. In this dataset, adsorption/binding energy is the predicted property, calculated using the total electronic energies from the reported dataset as follows:

$$E_{bind} = E_{ads/surf} - (E_{surf} + E_{ads})$$

We generated a second dataset to study CO_2 hydrogenation to methanol on Ni-Ga-based systems[70]. It includes Ni-fcc, Ni_3Ga-fcc, and Ni_5Ga_3-orthorhombic systems. Two surface types were considered for modeling the slab: flat surfaces (Ni(111), $Ni_3Ga(111)$, and $Ni_5Ga_3(221)$), and stepped surfaces (Ni(211), $Ni_3Ga(211)$, and $Ni_5Ga_3(211)$). For $Ni_3Ga(211)$ and $Ni_5Ga_3(211)$, two-step compositions were evaluated, one with a higher Ni concentration and another with a mixed Ni-Ga composition. Table S1 in the ESI contains side views of each proposed surface model. The key intermediates studied include the following adsorbates: C*, O*, HCOO*, and CH_3O*. This dataset accounts for two important factors: firstly, the adsorption of bidentate adsorbates, such as HCOO*, and secondly, reactions that depend on multiple adsorbates. Like the first dataset, only the relaxed geometries of clean metallic surfaces and free adsorbates in the gas phase were used to generate atomic descriptors. The predicted property is the electronic reaction energy, calculated as follows:

$$E_{reac} = \sum E_{products} - \sum E_{reactants} = \sum E_{products} - (E_{CO_2} + 3E_{H_2})$$

All reaction energies in this dataset are calculated using CO_2 and H_2 as common reference energies. The resulting dataset contains a total of 6708 reaction energy data points. Figure 1 shows the reaction scheme of each reaction step considered in this dataset, where only those appearing within the large blue box are included.

Workflow

We propose a methodology that integrates a structured workflow and an ML-based architecture to generate a predictive model to accelerate the exploration of binding interactions on bimetallic alloys. This approach accounts for key factors such as diverse alloy compositions, various adsorbates, complex binding interactions (including bidentate adsorbates), and binding properties influenced by multiple adsorbates. Given the need for a detailed representation of local adsorption sites, GNN-based architectures were selected for their ability to capture the chemical nature of these interactions effectively. Regardless of the specific binding property being predicted (e.g., adsorption or reaction energy), a standardized workflow was established to develop the predictive model, as shown in Fig. 2a. In our predictive model, the approach is based on the interaction between the metallic local adsorption site and the adsorbate. To define what constitutes the local site on the catalyst, we established a methodology to limit the region considered. Specifically, we first identify the atom or atoms in the adsorbate that are mainly bonded to the surface. Once the atoms constituting the local site are identified, the next step is constructing the graph representation for each data point. During this process, we also define the atomic features, which consist of a combination of tabulated atomic properties and easily accessible electronic descriptors obtained from DFT calculations. With the graph

representations ready, the GNN-based model is trained using the architecture presented in Fig. 2b.

Graph representation

A graph ($G = (V, E)$) is a mathematical structure used to represent relationships between entities, where V denotes the set of nodes (or vertices) representing individual elements, and E denotes the set of edges (or links) representing the connections or interactions between them. In chemical systems, nodes represent atoms, and edges represent the bonds or interactions between neighboring atoms. One essential characteristic of the graphs is that edges can be either directed or undirected. In directed graphs, edges have a specific direction, meaning they go from one node to another, but not necessarily the reverse. In contrast, undirected graphs have edges without direction, representing mutual connections. In this study, undirected graphs are employed. Additionally, both nodes and edges can be associated with features or attributes that provide more information about the modeled system. A key characteristic of graphs is their flexibility: unlike traditional fixed-size vector inputs used in machine learning, graphs can vary in size and shape, making them ideal for modeling complex, non-Euclidean structures like molecules, surfaces, or catalysts.

Constructing the graph representation involves defining a list of nodes (atoms) and identifying their neighboring atoms. As shown in the workflow (Fig. 2a), the local adsorption site is determined by identifying the atoms in the adsorbate that are primarily bonded to the surface. This typically involves a single atom for monodentate adsorbates, while two atoms are considered for bidentate adsorbates. This approach can be progressively extended to adsorbates with multiple bonding atoms. Once these key atoms are identified, cutoff spheres with a radius of 4.5 Å are centered on them to limit the region considered as the local adsorption site, as illustrated in Fig. 2c. The atoms enclosed within these cutoff spheres form the list of nodes, resulting in a substructure used to build the graph, as shown in Fig. 2d.

The next step is to define the list of neighboring atoms. One option could be to use all interatomic distances within the substructure and assume that all atoms are neighbors. However, we use a connectivity matrix to simplify the model and avoid reliance on the relaxed geometries of the adsorbate-surface system. This matrix is symmetric and binary - it contains a value of one when two atoms are considered neighbors, and zero otherwise, making the resulting graph undirected. In our case, two atoms are connected if the distance between them is smaller than the natural cutoff, as defined by the Atomic Simulation Environment (ASE) library[71]. This natural cutoff is based on the sum of the covalent radii of the two atoms, multiplied by a factor of 1.1, ensuring that only first-

neighbor interactions are captured. For the node features, we concatenate different properties in a single feature array per node, employing atomic tabulated features, electronic properties, and categorical features by type of adsorbate and surface. The tabulated properties defined for each node are atomic number, covalent radius, and Pauling electronegativity. We extract atomic electronic features such as the orbital occupancies (*s*, *p*, *d*, and *f*) from the DFT calculations of the clean surface and gas-phase adsorbates. The categorical concatenated features depend on whether the node represents a metal atom (surface atoms) or not. The average work function of the surface is only assigned to each node associated with the surface atoms, while the HOMO-LUMO gap energy of the adsorbate is only concatenated for the nodes representing adsorbate atoms. As a surface's global property, the work function encodes the surfaces by their stoichiometry, whereas the HOMO-LUMO gap encodes adsorbates by type. Lastly, we include one numerical feature for encoding the surface exposed facet (namely 'Step'). This feature is assigned at the substructure level, meaning all nodes within a given datapoint share the same numerical value.

Model architecture

The model was implemented using the PyTorch library[72], specifically PyTorch Geometric[73], a sub-library designed for building and training Graph Neural Networks (GNNs)[74]. The architecture of the GNN-based model (Fig. 2b) consists of three Graph Embedding Layers (GELs), a pooling layer, and a final linear transformation. For the GELs, we employed the GraphSAGE operator[75] to embed the node attributes. This operator was selected after comparing it to other alternatives, including GCNConv[74], GraphConv[76], and GATConv[77]. GraphSAGE achieved the highest predictive accuracy, as shown in Table S2 of the ESI. With the implementation of GNN based on Embedding Layers, it is essential to note that the dimensionality of the graph representation changes as it passes through the Graph Embedding Layers (GELs). Initially, the input has dimensions of (V_i, 8), where V_i is the number of atoms (nodes) in each graph and *8* is the number of features per node. After processing through the GELs, the dimensionality becomes (V_i, *hidden_dimension*), where *hidden_dimension* (or *output_dimension*, 512 (Alloys dataset)/256 (Ni-Ga dataset)) is a tunable hyperparameter. Finally, the *global_max_pool operator* is applied to reduce the variable-sized output from the GELs to a fixed-size 1D array (Euclidian space), by selecting the maximum value for each feature across all nodes, with a size of (1, *hidden_dimension*). The resulting embeddings in Euclidean space serve two purposes in our framework: (i) regression of target properties via a linear transformation layer in PyTorch, and (ii) clustering analysis for model interpretability. The model was trained using the Mean Squared Error (MSE) as the loss function and the Adam optimizer for stochastic weight optimization. After training, the

model's performance was evaluated using both Mean Squared Error and R^2 score on the training and test sets. To interpret the model and analyze the importance of each feature, we used GNNExplainer, an explainer tool available in PyTorch Geometric.

We also applied the Uniform Manifold Approximation and Projection (UMAP) technique[78] to reduce the dimensionality of the outputs from the pooled graph embeddings, allowing us to explore their correlation with the predicted binding properties. A detailed description of the hyperparameters used to train each ML-based model is provided in Table S3 of the ESI.

Model performance: Adsorption energies

As mentioned, the alloy's dataset consists of A_nB_m bimetallic systems, focusing exclusively on flat surfaces with an FCC Bravais lattice, comprising 17,343 datapoints. The stoichiometric ratio in this dataset is systematically varied, allowing the electronic structure of each catalyst to be analyzed based on the local geometry of the adsorption site, as illustrated in Fig. 3. The influence of composition on local sites is studied in conjunction with the binding behavior of adsorbates of different chemical natures; these adsorbates have different main bonded atoms at the surface, such as H, C, N, or O. In a previous study[69], we demonstrated that predictive models based on classical machine learning architectures can effectively capture these effects when used to estimate adsorption energies. In addition, we compared various classical ML architectures for predicting adsorption energies of monodentate adsorbates using the alloy's dataset. Among them, the CatBoost model demonstrated the best performance. The descriptors used in the previous study were constructed using an approach similar to the GNN model: cutoff spheres were added to define the local adsorption site. However, in the case of the classical ML architectures, the atomic properties of the surface atoms within the sphere are averaged to form the surface features. For the adsorbate, the features are defined by the properties of its main bonded atom on the surface. These two feature arrays are then concatenated into a single fixed-shape input array, which is used by the CatBoost model.

In the present work, we compare the CatBoost with the GNN-based architecture. Using the best-performing hyperparameters reported in the previous work, we retrained the model with an 70:15:15 train-validation-test split. To compare the performance of the CatBoost and GNN models, parity plots between the ML-predicted and DFT-calculated values were generated (see Fig. 4). As shown in Fig. 4a, the CatBoost model exhibited more biased predictions, particularly in the energy range of 0 to -4 eV, ranging from non-binding to weak adsorption energies. Previous analysis indicated that this bias originated from the inability of the model to fully capture binding interactions at top sites, due to the limitations of the fixed-structure descriptor methodology used in the CatBoost

architecture. In contrast, the results from the GNN-based model (Fig. 4b) show a clear reduction in data dispersion for both the training and test sets. Unlike the CatBoost model, the GNN model does not exhibit significant bias within the 0 to -4 eV energy range.

Extending the comparison between the CatBoost and GNN models. We calculated the Mean Squared Error (MSE) and the coefficient of determination (R²), as presented in Table 1. On the training set, the CatBoost model demonstrated a slightly lower MSE. Both models had similar R² scores, indicating that they performed comparably in correlating the proposed input features and the predicted adsorption energies for the training set. Nevertheless, more significant differences emerged when evaluating the models on the validation and testing sets. The MSEs for the CatBoost model were nearly twice those of the GNN-based model, as can also be graphically noticed in Fig. 4. Similarly, the R² score for CatBoost dropped considerably, indicating that the GNN model delivers stronger and more consistent predictive performance.

A main difference between the two models which explains the improve performance of the GNN-based architecture is in how features are represented. In the GNN model, attributes are assigned per node, preserving atomic-level detail. In contrast, the CatBoost model relies on averaged properties, reducing the chemical information to fixed-shape descriptors. Both models used geometrical, atomic tabulated, and electronic features. In the GNN model, the geometrical information is derived from the neighbor list (spatial relationship) and is also implicitly captured through the electronic properties. However, a notable advantage of the GNN approach is its ability to differentiate atoms based on their spatial position, such as distinguishing surface-exposed atoms from those deeper within the surface's structure, through electronic descriptors by atom (node). This distinction is especially valuable in surface modeling, as the lower coordination of the surface-exposed atoms is expected to be less stable than bulk atoms. Considering the other features employed, such distinctions cannot be captured wholly in averaged or tabulated atomic properties.

Table 1
Summary of the performance of the evaluated ML-based architectures for the alloy's dataset, including the metric of the average error and R^2 score for both the training, testing, and validation datasets: Mean Squared Error (MSE), and R^2 score.

ML-based models	MSE of train[eV]	R^2 score of train	MSE of test[eV]	R^2 score of test	MSE of validation[eV]	R^2 score of validation
CatBoost	0.067	0.983	0.415	0.894	0.372	0.904
GNN	0.073	0.982	0.181	0.954	0.215	0.945

An essential aspect of the proposed methodology is the correlation between physicochemical properties and binding interactions, where the selected features were chosen to ensure the model is grounded in physical and chemical reasoning. To validate the effectiveness of these features in the GNN-based model and simultaneously gain deeper insight into how its architecture operates, we analyzed the impact of atomic features, as illustrated in Fig. 5. To assess the effect of the node attributes, we used the GNNExplainer, which identifies the nodes that most influence the model's predictions for each graph and indicates the contribution of each feature by node. This analysis was performed across all graphs in the training set, and the impacts were averaged by feature. In the first case, the average impact was calculated by considering all nodes within each graph (Fig. 5a). This reveals that atomic radius and electronegativities are the most influential, both showing comparable and significant effects on the predicted adsorption energies. In contrast, work function and atomic number have the lowest impact, although their contributions are not negligible.

When examining the influence of orbital occupancies, the trend follows a decreasing order of $p > d > s$, while the *f*-orbitals (not plotted) show almost no contribution. To better understand this trend, we evaluated the feature's impact separately for surface and adsorbate atoms. For surface atoms (Fig. 5b), a similar pattern and magnitude of influence were observed, with *p*- and *d*-orbital occupancies again having the most significant impact on predicted energies. This finding aligns with the composition of the dataset, which includes elements from both the *d*-block and *p*-block. Following these, the *s*-orbital occupancy feature appears next in importance. Lastly, the step termination, atomic number, and work function show the lowest influence among the features of the surface atom. The step termination and work function features showed the lowest impact, likely because the dataset includes only two exposed facets. For adsorbate atoms (Fig. 5c), the feature impacts are more pronounced, indicating that the type of adsorbate has a more substantial influence on the predicted energy in the GNN-based model compared to the atoms in the bimetallic surfaces. The electronegativities show the highest impact, followed by the *s*-orbital occupancies. The observed trend in orbital occupancies ($s- > p-$) for the adsorbates is expected, as most of them contain hydrogen atoms. Consequently, the number of hydrogen atoms in each adsorbate helps distinguish between different types of molecules, as the *sp*-orbital hybridization changes proportionally with the number of hydrogen atoms.

By analyzing the impact of each feature, we were able to compare the importance of combining descriptors of different natures, specifically the combination of atomic electronic, atomic tabulated, and averaged properties. However, this analysis alone does not provide enough information. Therefore, we performed a clustering analysis to better understand the correlation between the proposed features and the adsorption energy. To conduct this analysis, it was first necessary to define the basic structure of the GNN

architecture. Node attributes are initially embedded through Graph Embedding Layers using the GraphSAGE and *global_max_pool* operators, producing values in the latent space. Then, a final linear transformation is applied to these embedded features to predict the adsorption energy. Using this framework, we extracted the latent space representations, i.e., the embedded node features, and applied UMAP for dimensionality reduction to project them into 2D. Figure 6a illustrates the correlation between the 2D reduced features and the adsorption energy. The resulting clusters reveal that the value of adsorption energies determines the clusters' distribution, i.e., the global structure. Furthermore, it is observed that clusters associated with the strongest binding interactions (indicated by dark blue points) are closely grouped, whereas clusters corresponding to weaker interactions are more spread out. This suggests that internal factors, properties, or features influence the relative proximity or separation of the clusters.

Additional properties were analyzed within the cluster visualization to understand which internal factors influence cluster proximity (global structure). Since the graph representation relies primarily on the node attributes, we identified the *i*-th node corresponding to the adsorbate's atom, mainly bonded on the surface, and extracted its atomic number and *s*-orbital occupancy. The atoms considered include H, C, N, O, and S. These values were then plotted using the 2D-reduced features, as shown in Fig. 6b and 6c. In Fig. 6b, each cluster was additionally assigned to its corresponding adsorbate. This assignment was based on combining *s*- and *p*-orbital occupancies (see Fig. S1 in the ESI). The clustering proximity indicates that the bonding interactions are more similar for adsorbates such as C, N, and O, which aligns with the closeness of these elements in the periodic table. Although S is not as close, its bonding interactions are still relatively similar to those of C, N, and O. In contrast, H forms a distinct cluster, reflecting its weaker bonding strength. Moreover, the presence of hydrogen in C-, N-, and O-based species reduces the similarity in bonding strength, causing the corresponding clusters to be more distant.

As previously mentioned, the sharpness and proximity of the clustering distribution are primarily determined by the type of adsorbate. However, this does not directly explain the trend in bonding strength for adsorbate-metal interactions. To better understand when this bonding is stronger or weaker, examining additional properties, specifically those related to the bimetallic surfaces, is necessary. For this purpose, we selected all nodes corresponding to metal atoms and averaged their features. Among the compared features, the *d*-orbital occupancy showed the strongest correlation with adsorption energy values, as illustrated in Fig. 6d. The results suggest a trend in which surfaces with lower *d*-orbital occupancy exhibit stronger adsorbate binding.

Furthermore, *d*-orbital occupancy tends to decrease as the average atomic radius of the metal atoms increases (see Fig. S2 in the ESI), i.e., for heavier elements. This trend implies that higher concentrations of heavier metal atoms may enhance bonding strength, potentially leading to strong chemisorption. Conversely, a higher concentration of lighter metals may result in weaker physisorption and short adsorbate residence times.

Model performance: Reaction energies

The comparison between the CatBoost and GNN architectures helps evaluate each model's performance and assess whether our selection of atomic features is appropriate for representing the local adsorption site. However, using this dataset also raises several questions regarding limitations that must be addressed when modeling more complex interactions. These include handling bidentate or multi-site adsorptions, capturing the dependence of multiple adsorbates on the predicted properties, how the model is affected when higher Miller index surfaces are included, and distinguishing between structurally similar adsorbates. To further explore these challenges, we used an in-house obtained dataset focused on predicting electronic reaction energies for various carbon-based adsorbates[70], corresponding to reaction intermediates on Ni-Ga surfaces, explicitly focusing on Ni, Ni_3Ga, and Ni_5Ga_3 systems, comprising a total of 6,708 reaction energy datapoints. The catalytic performance for methanol production has been previously discussed. In our previous joint experimental and computational work, Ni_3Ga was evaluated as a methanol synthesis catalyst from CO_2 and H_2 and compared to other Ni-based systems in a joint experimental and theoretical effort. Nevertheless, it proved computationally challenging to establish correlations with global surface properties such as the work function or *d*-band center with the reaction energies. This limitation indicated that local descriptors were necessary to fully capture the bonding interactions of the reaction intermediates of the CO_2 hydrogenation to methanol adsorbed on Ni-Ga-based surfaces.

Developing a predictive model that relates reaction energies to the local chemical structure of these adsorption sites can provide valuable insights into which catalytic properties are responsible for modulating catalytic activity. Furthermore, the composition and Bravais lattice of the exposed facet of Ni_5Ga_3 exhibit more heterogeneous adsorption sites, meaning it contains a greater variety of distinct local adsorption sites, increasing the complexity of modeling this catalyst (see Fig. 7). Using the same type of atomic features applied in the bimetallic alloy's dataset, we trained a GNN-based model. The parity between DFT-calculated and ML-predicted reaction energies is shown in Fig. 8. Compared to the adsorption energy model, the GNN-based model for reaction energies demonstrates excellent performance, with no highly biased predictions observed over the entire energy range.

To complement the results shown in the parity plot, the accuracy metrics are summarized in Table 2. The near-zero Mean Squared Error for the training, validation, test sets, and coefficients of determination (R^2) close to one confirm that the model shows minimal deviation from the DFT-calculated reaction energies in the Ni-Ga dataset. While this dataset is more homogeneous since it is limited to Ni-Ga surfaces and therefore a good performance is expected, it is important to note that it also includes complex local environments. These complexities arise from the presence of stepped surfaces, which introduce structural diversity and pose additional challenges for prediction. Another important consideration is that some reaction energies depend on two or three adsorbates. In the proposed methodology, this multi-adsorbate dependence is addressed by concatenating the graph representations of each adsorbate into a single data point, i.e., by generating a separate connectivity matrix for each adsorbate and then combining them.

Table 2
Summary of the performance of the GNN-based architecture for the Ni-Ga dataset, including the metric of the average error and R^2 score for both the training and testing datasets: Mean Squared Error (MSE), and R^2 score.

ML-based models	MSE of train[eV]	R^2 score of train	MSE of test[eV]	R^2 score of test	MSE of validation[eV]	R^2 score of validation
GNN	0.001	0.999	0.002	0.998	0.001	0.999

Similar to the analysis performed on the alloy's dataset, the impact of atomic features on the GNN-based model was evaluated. In this case, the analysis was only performed for the surface and the adsorbate atoms (see Fig. 9), as averaging the feature impact across all atoms did not provide sufficient insight. The average impact for the surface atoms is shown in Fig. 9a. The most influential feature is the atomic radius, which is consistent with the adsorption energy model; however, its impact is slightly higher in this case. In contrast, the second most influential feature is the atomic number for the surface atoms, unlike in the alloy's dataset, where it had one of the lowest impacts. In descending order are *d*-orbital occupancy, the work function, electronegativity, and *p*-orbital occupancy, all of which have a moderate impact. In ascending order, the features with the least influence are step termination and *s*-orbital occupancy. The step termination and work function are categorical features intended to encode the exposed facet and surface type. Both are global surface descriptors, meaning they are not defined locally for individual atoms but remain identical for all nodes within a given substructure. However, in this dataset, the average work function of the clean surface appears to be more effective in distinguishing surface types than step termination when the surface atoms are considered, suggesting that the current encoding method for the step termination feature may be insufficient to differentiate between surface configurations fully.

Regarding the adsorbate atoms, the impact of their features was also evaluated, as shown in Fig. 9b. Similar to the alloy dataset, adsorbate-related features exhibit a greater influence than surface atoms. This confirms that, in the proposed GNN-based models, the bonding interaction between the adsorbate and the metal is highly dependent on the type of adsorbate. The atomic radius has the highest impact among the adsorbate features, followed by *s*-, *p*- orbital occupancies, step termination, atomic number, HOMO-LUMO energy, and electronegativity. Unlike the model for predicting adsorption energies, the GNN model shows that electronic atomic features contribute more significantly than tabulated atomic properties. This difference may stem from the fact that most adsorbates in the Ni-Ga dataset are carbon-based, making it more challenging to differentiate them using only tabulated properties. Finally, although the electronegativity feature is not among the most impactful, its influence is still greater than that of the surface atom features.

Then, we performed a clustering analysis on the embedded features for the Ni-Ga dataset. The visualization of the reduced features alongside the reaction energies is shown in Fig. 10a. For clarity, reaction energies higher than 4 eV are excluded from the plot, but this is only for the visualization. Compared to the alloy's dataset, the clusters in the Ni-Ga system are smaller and more dispersed, indicating fewer similarities among the clusters. This distribution cannot be attributed to the type of adsorbate, as most clusters correspond to the formation of C* + 2O* (see Fig. S3 in the ESI). At the same time, the remaining intermediates are grouped within a smaller region.

Additionally, the work function and step termination were included when evaluating other influential descriptors on the visualization of the 2D reduced features. These features contribute to distinguishing and grouping surfaces by stoichiometry and atom coordination, reflecting the catalyst's structure (see Figs. S4 and S5 in the ESI). To better understand the factors influencing bonding strength, we analyzed the reaction involving the formation of C* + 2O*. This reaction step correlates with the average atomic radius of the surface atoms (see Fig. 10b); the reaction energy increases with a larger average atomic radius of the surface atoms, corresponding to a higher concentration of Ga. This correlation also reflects the dependence of bonding on *d*-orbital occupancy, as shown in Fig. S6. In the context of CO_2 hydrogenation to methanol, forming C* is undesirable since it leads to side reactions. Therefore, increasing the Ga concentration can be favorable, using a catalyst like Ni_5Ga_3, as it reduces the selectivity toward C* and promotes methanol formation.

The separate analysis of the impact from surface and adsorbate atoms reveals general trends in how features correlate with predicted energies. However, some specific insights can be overlooked when the impacts are averaged. Therefore, performing a per-atom analysis helps to capture these finer details. To illustrate this, we analyzed the graph

representations of two specific HCOO* adsorption structures, one with the lowest reaction energy (Fig. 11a) and one with the highest (Fig. 11c), corresponding to the most stable and least stable configurations. For the most stable structure, we also present a heatmap showing the impact of each atom (Fig. 11b). This heatmap indicates that, once again, the atoms with the highest impact belong to the adsorbate (atoms with index from 12 to 15). In particular, the *s*- and *p*-orbital occupancies and electronegativities contribute most to the model's prediction. Regarding the surface atoms, fewer atoms influence the reaction energy in this configuration, particularly those of the adsorbate. We found that the Ni atoms (specifically atoms with index 6 and 11), which are directly bonded to the adsorbate, have a greater impact on the bonding interaction than other metal atoms.

For the least stable HCOO structure (Fig. 11c), the corresponding heatmap showing the impact of features per atom is presented in Fig. 11d. Ga with index 2 presents a high impact on the reaction energy among the surface atoms. These results suggest that the direct bonding of HCOO* to one Ga atom, along with a higher overall Ga presence, increases the reaction energy and contributes to the instability of this configuration. Considering possible methanol formation pathways, one proposed route involves the formation of HCOO*. In this case, we found that increasing the Ga concentration decreases the stability of HCOO*, particularly in systems like Ni_5Ga_3. This suggests that precise control over the catalyst's stoichiometry is necessary to regulate both C* and HCOO* formation effectively, and geometrical factors, such as the coordination, can play a huge role. Fig. S7 shows the distribution of reaction energies for each step in a violin plot. These results highlight the importance of the local adsorption site composition, which is consistent with the findings from the clustering analysis.

DISCUSSION

This paper proposes a methodology for training a GNN-based architecture that relies solely on graph representations with node attributes, avoiding edge attributes. The first section compares two machine learning architectures: the proposed GNN model and CatBoost, which uses fixed-shape arrays as input. For the comparison, predictive models were trained to estimate adsorption energies using a dataset of A_nB_m bimetallic alloys. The results confirm that the graph-based representation is more suitable for capturing the local adsorption site and effectively modeling the adsorbate-bimetallic catalyst binding interactions. In the CatBoost model, the local adsorption site is represented as a fixed input array that combines the averaged properties of the surface metal atoms with those of the adsorbate atoms. Additional geometric features were included to distinguish different binding modes in the CatBoost model, such as coordination number and the number of metal atoms bonded to the adsorbate. However, our reported results suggested that this approach falls short in accurately capturing binding interactions, particularly for

bonding on top sites[69]. In contrast, the graph-based representation inherently includes geometric information through the connection matrix, eliminating the need for explicitly defined geometric features. A comparison of the most biased data points between the two models reveals that the GNN more effectively captures top-site adsorption modes.

Our proposed node-based features can be categorized into three types: (1) average properties that describe the surface or adsorbate by type, such as step termination and work function for surfaces, or HOMO-LUMO energies for adsorbates; (2) tabulated atomic properties, including atomic number, atomic radius, and electronegativity; and (3) electronic properties per atom, such as orbital occupancies. The combination of these node attributes is intended to achieve a highly accurate predictive model and enable clustering analyses that reveal clearer and more specific correlations between features and predicted properties, thereby facilitating a deeper understanding of adsorbate-metal interactions. Upon evaluating the correlation and performance of the proposed models, we found that while average properties fulfill their intended role, they have the lowest overall impact on the model. Moreover, none of these average properties alone can fully differentiate data points based on surface type. However, combining step termination and work function features helps to alleviate this limitation.

The tabulated atomic properties generally show the highest impact in GNN-based models, indicating that differences highly influence this type of architecture in node (atom) type. This result is consistent with previous studies, where models using only atomic number as a feature have achieved high accuracy[55], and other GNN-based models, such as CGCNN[42], which encodes several atomic properties and bond distances, have also demonstrated strong performance. However, it is essential to highlight that, in our case, electronegativity and atomic radius have the highest impact. This is significant because these features help differentiate atom types and capture underlying physicochemical properties. Unlike the atomic number, features such as electronegativity and atomic radius reflect the periodic trends of elements, offering the model more chemically meaningful information.

Including features that account for the electronic structure of adsorbates and surfaces significantly impacts both models, improving their ability to distinguish between different types of surfaces and adsorbates. These features were included to capture electronic trends relevant to adsorbate-metal interactions, thus describing how adsorbates bind to metal surfaces. Beyond this purpose, electronic atomic features could also help differentiate between adsorbates more effectively. For example, they can reflect subtle atomic differences in bond activation or transition states, where tabulated atomic properties alone would not provide sufficient detail. Another aspect of the GNN-based model is that bond attributes are not used in the graph representation. Notably, electronic features allow the model to distinguish between surface-exposed and subsurface metal

atoms. This is especially beneficial for capturing more complex atomic coordination environments, such as those in high Miller index surfaces.

Although it is possible to include bond distances in the model to improve accuracy, we chose not to do so, in contrast to other studies using the same bimetallic alloy dataset with graph representations based on node and edge attributes (bond distances)[50]. Following the proposed approach of Pablo-García et al.[55], our model is designed for quick and wide screening of bonding interactions in bimetallic catalysts and therefore relies only on easily accessible properties. With this approach, once the model is trained, only DFT calculations for the clean surface and gas-phase adsorbate are needed, eliminating the need for computationally expensive relaxed adsorbate-surface structures. This methodology can also be extended to larger and more complex molecules, for which DFT relaxation becomes the most resource-intensive step. Although the type of adsorbate generally influences the binding energy in both datasets, accurately capturing the structural information of the local adsorption site plays a more significant role in determining the bonding strength. This effect is particularly evident in the Ni-Ga dataset, where the coordination and abundance of Ga atoms lead to either stronger or weaker interactions, furthermore, when analyzing the interactions of individual adsorbates (e.g., C* and HCOO*) at a local level, it becomes clear that proposing generalizable trends may overlook critical details about the local structure, resulting in a loss of valuable information regarding catalytic activity.

In this contribution, we presented an approach to generate graph representations for predicting binding interactions in bimetallic systems with high accuracy. Our results demonstrate the strength of this method compared to traditional ML-based architectures that require fixed input representations. The flexibility of GNN-based models allows them to fully capture complex aspects that are difficult to represent in Euclidean space, such as mono- and bi-dentate interactions, without increasing the data sparsity. Additionally, this approach enables the inclusion of graph-based representations for properties that depend on multi-adsorbate interactions, and it can model highly complex local adsorption sites, such as those found on high Miller index surfaces, without omitting atomic information. Finally, this approach is presented as a tool to analyze graph representations and uncover physicochemical trends that can accelerate the exploration of bimetallic alloy catalysts, via explainable feature impact and clustering analysis. This methodology enables the development of a GNN-based predictive model for adsorption energies that outperforms the CatBoost approach, achieving mean squared errors (MSE) of 0.073 eV for the training set and 0.181 eV for the test set. A second model was also trained for reaction energies, reaching respective MSE values of 0.001 eV and 0.002 eV for the training and test sets. The proposed node attributes, based on easily accessible atomic and electronic features, allow the model to go beyond the limitations of using atomic numbers alone in graph

representations. In both models, these features enable a deeper understanding of the binding trends on adsorbate-metal interactions.

METHODS

Computational details

As mentioned, two datasets were used, with calculations performed within the periodic Density Functional Theory (DFT) framework, though each dataset was obtained using a different DFT code. For the first dataset, which consists of bimetallic alloys used to calculate adsorption energies, simulations were conducted using Quantum ESPRESSO, a plane-wave-based DFT code[79,80]. The computational parameters were previously reported on our former ML-based model, which employed the CatBoost architecture. A more detailed description of the DFT parameters can be found in our previous work [69]. The alloy dataset was extracted from a previously reported dataset on Catalysis-Hub, and the calculation parameters were adapted accordingly[66]. For this dataset, spin-polarized calculations were performed using the BEEF-vdW[81] functional.

The second dataset consists of NiGa alloys, used to calculate reaction energies of key intermediates in CO_2 hydrogenation to methanol. This dataset was obtained using the Vienna Ab initio Simulation Package (VASP), another plane-wave-based DFT code[82–84]. The DFT parameters are the same as those in our previously reported study, which analyzed the energetic profile of the most stable adsorption sites for the considered key intermediates. A more detailed description of the DFT parameters can be found in the referenced paper[70]. Like the first dataset, the BEEF-vdW[81] functional was used to calculate structure optimization and electronic properties.

Hyperparameter optimization

Each input graph considered only node attributes, i.e., only features per atom were employed. To prevent these attributes from having a disproportionate influence on predictions due to differences in scale, normalization was applied using the MaxAbsScaler transformation from Scikit-learn[85]. Each dataset was randomly divided into training, validation, and test sets with a 70:15:15 split ratio. The proposed architecture for the GNN model only has four controllable hyperparameters: batch size, output size, hidden dimension, dropout ratio, and learning rate. The evaluated batch sizes for the training were 16, 32, and 64. The output size or hidden dimension determines the number of outputs after the Graph Embedding Layer (GEL), with values ranging from 4 to 512, increasing exponentially at multiples of two. The dropout ratio, which reduces the number of outputs after a GEL to prevent overfitting, was varied from 0.1 to 0.9 in increments of 0.2. The learning rate was tested at 0.0005, 0.001, and 0.005 values. The best-performing

hyperparameters were selected to avoid over- and under-parameterization, ensuring the lowest Mean Squared Error (MSE) for both training and test sets.

Declarations

CONFLICT OF INTEREST

The authors declare that the research was conducted without commercial or financial relationships that could be construed as a potential conflict of interest.

FUNDING

The authors thank the Spanish "Ministerio de Ciencia e Innovación" for funding the "I + D Generación del Conocimiento" project (PID2021-128416NB-I00 and PGC2018-100818-A-I00) and the predoctoral grant (PRE2019-089605). A part of the work has been performed under Project HPC-EUROPA3 (INFRAIA-2016-1-730897), with the support of the EC Research Innovation Action under the H2020 Programme awarded to CSP.

Author Contribution

A. F. Usuga: data curation, formal analysis, investigation, methodology, implementation of code, validation, visualization, writing (original draft), writing (review & editing). C. S. Praveen: conceptualization, data curation, supervision, writing (review & editing). A. Comas-Vives: data curation, conceptualization, project administration, resources, funding acquisition, methodology, supervision, validation, writing (review & editing).

ACKNOWLEDGMENTS

DFT calculations were partially performed in the HPC "Consorci de Serveis Universitaris de Catalunya (CSUC)". The authors thank the Spanish "Ministerio de Ciencia e Innovación" for funding the "I + D Generación del Conocimiento" project (PID2021-128416NB-I00 and PGC2018-100818-A-I00) and the predoctoral grant (PRE2019-089605). CSP acknowledges Cochin University of Science and Technology for the SMNRI project grant.

Data Availability

The ML-based models are available in the GitHub repository; address inside the parenthesis (https://github.com/anfeus/Localized-chemical-E_ads-GNN).A preprint of this work has been deposited on ChemRxiv; address inside the parenthesis (https://doi.org/10.26434/chemrxiv-2025-s2p1s).

References

1. *Springer Handbook of Nanomaterials*; Vajtai, R., Ed.; Springer Berlin Heidelberg: Berlin, Heidelberg, 2013. https://doi.org/10.1007/978-3-642-20595-8.
2. Mistry, H.; Varela, A. S.; Kühl, S.; Strasser, P.; Cuenya, B. R. Nanostructured Electrocatalysts with Tunable Activity and Selectivity. *Nat Rev Mater* 2016, *1* (4), 16009. https://doi.org/10.1038/natrevmats.2016.9.
3. Vogt, C.; Weckhuysen, B. M. The Concept of Active Site in Heterogeneous Catalysis. *Nat Rev Chem* 2022, *6* (2), 89–111. https://doi.org/10.1038/s41570-021-00340-y.
4. Chen, B. W. J.; Mavrikakis, M. Modeling the Impact of Structure and Coverage on the Reactivity of Realistic Heterogeneous Catalysts. *Nat Chem Eng* 2025, *2* (3), 181–197. https://doi.org/10.1038/s44286-025-00179-w.
5. Medford, A. J.; Vojvodic, A.; Hummelshøj, J. S.; Voss, J.; Abild-Pedersen, F.; Studt, F.; Bligaard, T.; Nilsson, A.; Nørskov, J. K. From the Sabatier Principle to a Predictive Theory of Transition-Metal Heterogeneous Catalysis. *Journal of Catalysis* 2015, *328*, 36–42. https://doi.org/10.1016/j.jcat.2014.12.033.
6. Ooka, H.; Huang, J.; Exner, K. S. The Sabatier Principle in Electrocatalysis: Basics, Limitations, and Extensions. *Front. Energy Res.* 2021, *9*. https://doi.org/10.3389/fenrg.2021.654460.
7. Abild-Pedersen, F.; Greeley, J.; Studt, F.; Rossmeisl, J.; Munter, T. R.; Moses, P. G.; Skúlason, E.; Bligaard, T.; Nørskov, J. K. Scaling Properties of Adsorption Energies for Hydrogen-Containing Molecules on Transition-Metal Surfaces. *Phys. Rev. Lett.* 2007, *99* (1), 016105. https://doi.org/10.1103/PhysRevLett.99.016105.
8. Greeley, J. Theoretical Heterogeneous Catalysis: Scaling Relationships and Computational Catalyst Design. *Annu. Rev. Chem. Biomol. Eng.* 2016, *7* (1), 605–635. https://doi.org/10.1146/annurev-chembioeng-080615-034413.
9. Mamun, O.; Winther, K. T.; Boes, J. R.; Bligaard, T. A Bayesian Framework for Adsorption Energy Prediction on Bimetallic Alloy Catalysts. *npj Comput Mater* 2020, *6* (1), 177. https://doi.org/10.1038/s41524-020-00447-8.
10. Pérez-Ramírez, J.; López, N. Strategies to Break Linear Scaling Relationships. *Nat Catal* 2019, *2* (11), 971–976. https://doi.org/10.1038/s41929-019-0376-6.
11. Ulissi, Z. W.; Medford, A. J.; Bligaard, T.; Nørskov, J. K. To Address Surface Reaction Network Complexity Using Scaling Relations Machine Learning and DFT Calculations. *Nat Commun* 2017, *8* (1), 14621. https://doi.org/10.1038/ncomms14621.

12. Hammer, B.; Norskov, J. K. Why Gold Is the Noblest of All the Metals. *Nature* 1995, *376* (6537), 238–240. https://doi.org/10.1038/376238a0.
13. Hammer, B.; Nørskov, J. K. Electronic Factors Determining the Reactivity of Metal Surfaces. *Surface Science* 1995, *343* (3), 211–220. https://doi.org/10.1016/0039-6028(96)80007-0.
14. Yang, Z.; Gao, W. Applications of Machine Learning in Alloy Catalysts: Rational Selection and Future Development of Descriptors. *Advanced Science* 2022, *9* (12), 2106043. https://doi.org/10.1002/advs.202106043.
15. Mou, T.; Pillai, H. S.; Wang, S.; Wan, M.; Han, X.; Schweitzer, N. M.; Che, F.; Xin, H. Bridging the Complexity Gap in Computational Heterogeneous Catalysis with Machine Learning. *Nat Catal* 2023, *6* (2), 122–136. https://doi.org/10.1038/s41929-023-00911-w.
16. Hart, G. L. W.; Mueller, T.; Toher, C.; Curtarolo, S. Machine Learning for Alloys. *Nat Rev Mater* 2021, *6* (8), 730–755. https://doi.org/10.1038/s41578-021-00340-w.
17. Wei, J.; Chu, X.; Sun, X.; Xu, K.; Deng, H.; Chen, J.; Wei, Z.; Lei, M. Machine Learning in Materials Science. *InfoMat* 2019, *1* (3), 338–358. https://doi.org/10.1002/inf2.12028.
18. Zhang, D.; Zhang, Q.; Peng, C.; Long, Z.; Zhuang, G.; Kramer, D.; Komarneni, S.; Zhi, C.; Xue, D. Recent Advances in Developing Multiscale Descriptor Approach for the Design of Oxygen Redox Electrocatalysts. *iScience* 2023, *26* (5), 106624. https://doi.org/10.1016/j.isci.2023.106624.
19. Ding, R.; Chen, J.; Chen, Y.; Liu, J.; Bando, Y.; Wang, X. Unlocking the Potential: Machine Learning Applications in Electrocatalyst Design for Electrochemical Hydrogen Energy Transformation. *Chem. Soc. Rev.* 2024, *53* (23), 11390–11461. https://doi.org/10.1039/d4cs00844h.
20. Yang, Z.; Gao, W.; Jiang, Q. A Machine Learning Scheme for the Catalytic Activity of Alloys with Intrinsic Descriptors. *J. Mater. Chem. A* 2020, *8* (34), 17507–17515. https://doi.org/10.1039/D0TA06203K.
21. Li, X.; Li, B.; Yang, Z.; Chen, Z.; Gao, W.; Jiang, Q. A Transferable Machine-Learning Scheme from Pure Metals to Alloys for Predicting Adsorption Energies. *J. Mater. Chem. A* 2022, *10* (2), 872–880. https://doi.org/10.1039/D1TA09184K.
22. Datta, J.; Koratkar, N.; Datta, D. Unlocking the Potential of Open-Tunnel Oxides: DFT-Guided Design and Machine Learning-Enhanced Discovery for next-Generation Industry-Scale Battery Technologies. *Energy Adv.* 2024, *3* (5), 968–982. https://doi.org/10.1039/d4ya00014e.
23. Li, Z.; Wang, S.; Chin, W. S.; Achenie, L. E.; Xin, H. High-Throughput Screening of Bimetallic Catalysts Enabled by Machine Learning. *J. Mater. Chem. A* 2017, *5* (46), 24131–24138. https://doi.org/10.1039/C7TA01812F.

24. Mehrmohammadi, P.; Ghaemi, A. Investigating the Effect of Textural Properties on CO2 Adsorption in Porous Carbons via Deep Neural Networks Using Various Training Algorithms. *Sci Rep* 2023, *13* (1), 21264. https://doi.org/10.1038/s41598-023-48683-4.
25. Liu, X.; Chen, F.; Zhang, W.; Ma, F.; Xu, P. Machine Learning Models for Easily Obtainable Descriptors of the Electrocatalytic Properties of Ag-Pd-Ir Nanoalloys toward the Formate Oxidation Reaction. *Nanoscale* 2025, *17*, 2810–2819. https://doi.org/10.1039/d4nr03735a.
26. Xu, W.; Reuter, K.; Andersen, M. Predicting Binding Motifs of Complex Adsorbates Using Machine Learning with a Physics-Inspired Graph Representation. *Nat Comput Sci* 2022, *2* (7), 443–450. https://doi.org/10.1038/s43588-022-00280-7.
27. Jin, J.; Faraji, S.; Liu, B.; Liu, M. Comparative Analysis of Conventional Machine Learning and Graph Neural Network Models for Perovskite Property Prediction. *J. Phys. Chem. C* 2024, *128* (39), 16672–16683. https://doi.org/10.1021/acs.jpcc.4c03212.
28. Wang, Q.; Yao, Y. Harnessing Machine Learning for High-Entropy Alloy Catalysis: A Focus on Adsorption Energy Prediction. *npj Comput Mater* 2025, *11* (1), 91. https://doi.org/10.1038/s41524-025-01579-5.
29. Deng, D.; Lei, Z.; Hong, X.; Zhang, R.; Zhou, F. Describe Molecules by a Heterogeneous Graph Neural Network with Transformer-like Attention for Supervised Property Predictions. *ACS Omega* 2022, *7* (4), 3713–3721. https://doi.org/10.1021/acsomega.1c06389.
30. Flam-Shepherd, D.; Wu, T. C.; Friederich, P.; Aspuru-Guzik, A. Neural Message Passing on High Order Paths. *Mach. Learn.: Sci. Technol.* 2021, *2* (4), 045009. https://doi.org/10.1088/2632-2153/abf5b8.
31. Li, S.-W.; Xu, L.-C.; Zhang, C.; Zhang, S.-Q.; Hong, X. Reaction Performance Prediction with an Extrapolative and Interpretable Graph Model Based on Chemical Knowledge. *Nat Commun* 2023, *14* (1), 3569. https://doi.org/10.1038/s41467-023-39283-x.
32. Wu, Z.; Wang, J.; Du, H.; Jiang, D.; Kang, Y.; Li, D.; Pan, P.; Deng, Y.; Cao, D.; Hsieh, C.-Y.; Hou, T. Chemistry-Intuitive Explanation of Graph Neural Networks for Molecular Property Prediction with Substructure Masking. *Nat Commun* 2023, *14* (1), 2585. https://doi.org/10.1038/s41467-023-38192-3.
33. Reiser, P.; Neubert, M.; Eberhard, A.; Torresi, L.; Zhou, C.; Shao, C.; Metni, H.; Van Hoesel, C.; Schopmans, H.; Sommer, T.; Friederich, P. Graph Neural Networks for Materials Science and Chemistry. *Commun Mater* 2022, *3* (1), 93. https://doi.org/10.1038/s43246-022-00315-6.
34. Banik, S.; Dhabal, D.; Chan, H.; Manna, S.; Cherukara, M.; Molinero, V.; Sankaranarayanan, S. K. R. S. CEGANN: Crystal Edge Graph Attention Neural

Network for Multiscale Classification of Materials Environment. *npj Comput Mater* 2023, *9* (1), 23. https://doi.org/10.1038/s41524-023-00975-z.

35. Xie, T.; France-Lanord, A.; Wang, Y.; Shao-Horn, Y.; Grossman, J. C. Graph Dynamical Networks for Unsupervised Learning of Atomic Scale Dynamics in Materials. *Nat Commun* 2019, *10* (1), 2667. https://doi.org/10.1038/s41467-019-10663-6.
36. Fung, V.; Zhang, J.; Juarez, E.; Sumpter, B. G. Benchmarking Graph Neural Networks for Materials Chemistry. *npj Comput Mater* 2021, *7* (1), 84. https://doi.org/10.1038/s41524-021-00554-0.
37. Sunshine, E. M.; Shuaibi, M.; Ulissi, Z. W.; Kitchin, J. R. Chemical Properties from Graph Neural Network-Predicted Electron Densities. *J. Phys. Chem. C* 2023, *127* (48), 23459–23466. https://doi.org/10.1021/acs.jpcc.3c06157.
38. Jia, S.; Parthasarathy, A. R.; Feng, R.; Cong, G.; Zhang, C.; Fung, V. Derivative-Based Pre-Training of Graph Neural Networks for Materials Property Predictions. *Digital Discovery* 2024, *3* (3), 586–593. https://doi.org/10.1039/d3dd00214d.
39. Witman, M. D.; Goyal, A.; Ogitsu, T.; McDaniel, A. H.; Lany, S. Defect Graph Neural Networks for Materials Discovery in High-Temperature Clean-Energy Applications. *Nat Comput Sci* 2023, *3* (8), 675–686. https://doi.org/10.1038/s43588-023-00495-2.
40. Li, Q.; Fu, N.; Omee, S. S.; Hu, J. MD-HIT: Machine Learning for Material Property Prediction with Dataset Redundancy Control. *npj Comput Mater* 2024, *10* (1), 245. https://doi.org/10.1038/s41524-024-01426-z.
41. Feng, J.; Dong, Z.; Ji, Y.; Li, Y. Accelerating the Discovery of Metastable IrO2 for the Oxygen Evolution Reaction by the Self-Learning-Input Graph Neural Network. *JACS Au* 2023, *3* (4), 1131–1140. https://doi.org/10.1021/jacsau.2c00709.
42. Xie, T.; Grossman, J. C. Crystal Graph Convolutional Neural Networks for an Accurate and Interpretable Prediction of Material Properties. *Phys. Rev. Lett.* 2018, *120* (14), 145301. https://doi.org/10.1103/physrevlett.120.145301.
43. Bang, K.; Hong, D.; Park, Y.; Kim, D.; Han, S. S.; Lee, H. M. Machine Learning-Enabled Exploration of the Electrochemical Stability of Real-Scale Metallic Nanoparticles. *Nat Commun* 2023, *14* (1), 3004. https://doi.org/10.1038/s41467-023-38758-1.
44. Luo, Y.; Chen, H.; Wang, J.; Niu, X. Machine-Learning-Assisted Discovery of Boron-Doped Graphene with High Work Function as an Anode Material for Li/Na/K-Ion Batteries. *Phys. Chem. Chem. Phys.* 2023, *25* (17), 12200–12206. https://doi.org/10.1039/d3cp00669g.
45. Boonpalit, K.; Kinchagawat, J.; Prommin, C.; Nutanong, S.; Namuangruk, S. Efficient Exploration of Transition-Metal Decorated MXene for Carbon Monoxide Sensing Using Integrated Active Learning and Density Functional Theory. *Phys. Chem. Chem. Phys.* 2023, *25* (42), 28657–28668. https://doi.org/10.1039/d3cp03667g.

46. Ghanekar, P. G.; Deshpande, S.; Greeley, J. Adsorbate Chemical Environment-Based Machine Learning Framework for Heterogeneous Catalysis. *Nat Commun* 2022, *13* (1), 5788. https://doi.org/10.1038/s41467-022-33256-2.
47. Choudhary, K.; DeCost, B. Atomistic Line Graph Neural Network for Improved Materials Property Predictions. *npj Comput Mater* 2021, *7* (1), 185. https://doi.org/10.1038/s41524-021-00650-1.
48. Wei, C.; Shi, D.; Yang, Z.; Xue, Z.; Liu, S.; Li, R.; Mu, T. Data-Driven Design of Double-Atom Catalysts with High H2 Evolution Activity/CO2 Reduction Selectivity Based on Simple Features. *J. Mater. Chem. A* 2023, *11* (34), 18168–18178. https://doi.org/10.1039/d3ta02332j.
49. Louis, S.-Y.; Zhao, Y.; Nasiri, A.; Wang, X.; Song, Y.; Liu, F.; Hu, J. Graph Convolutional Neural Networks with Global Attention for Improved Materials Property Prediction. *Phys. Chem. Chem. Phys.* 2020, *22* (32), 18141–18148. https://doi.org/10.1039/d0cp01474e.
50. Omee, S. S.; Louis, S.-Y.; Fu, N.; Wei, L.; Dey, S.; Dong, R.; Li, Q.; Hu, J. Scalable Deeper Graph Neural Networks for High-Performance Materials Property Prediction. *Patterns* 2022, *3* (5), 100491. https://doi.org/10.1016/j.patter.2022.100491.
51. Deng, B.; Zhong, P.; Jun, K.; Riebesell, J.; Han, K.; Bartel, C. J.; Ceder, G. CHGNet as a Pretrained Universal Neural Network Potential for Charge-Informed Atomistic Modelling. *Nat Mach Intell* 2023, *5* (9), 1031–1041. https://doi.org/10.1038/s42256-023-00716-3.
52. Wander, B.; Musielewicz, J.; Cheula, R.; Kitchin, J. R. Accessing Numerical Energy Hessians with Graph Neural Network Potentials and Their Application in Heterogeneous Catalysis. *J. Phys. Chem. C* 2025, *129* (7), 3510–3521. https://doi.org/10.1021/acs.jpcc.4c07477.
53. Wander, B.; Shuaibi, M.; Kitchin, J. R.; Ulissi, Z. W.; Zitnick, C. L. CatTSunami: Accelerating Transition State Energy Calculations with Pretrained Graph Neural Networks. *ACS Catal.* 2025, *15* (7), 5283–5294. https://doi.org/10.1021/acscatal.4c04272.
54. Lan, J.; Palizhati, A.; Shuaibi, M.; Wood, B. M.; Wander, B.; Das, A.; Uyttendaele, M.; Zitnick, C. L.; Ulissi, Z. W. AdsorbML: A Leap in Efficiency for Adsorption Energy Calculations Using Generalizable Machine Learning Potentials. *npj Comput Mater* 2023, *9* (1), 172. https://doi.org/10.1038/s41524-023-01121-5.
55. Pablo-García, S.; Morandi, S.; Vargas-Hernández, R. A.; Jorner, K.; Ivković, Ž.; López, N.; Aspuru-Guzik, A. Fast Evaluation of the Adsorption Energy of Organic Molecules on Metals via Graph Neural Networks. *Nat Comput Sci* 2023, *3* (5), 433–442. https://doi.org/10.1038/s43588-023-00437-y.

56. Li, X.; Huang, W.; Lian, Y.; Tao, S. Graph Neural Network Model Accelerates Biomass Adsorption Energy Prediction on Iron-Group Hydrotalcite Electrocatalysts. *J. Phys. Chem. Lett.* 2024, *15* (42), 10725–10733. https://doi.org/10.1021/acs.jpclett.4c02466.
57. Deshpande, S.; Maxson, T.; Greeley, J. Graph Theory Approach to Determine Configurations of Multidentate and High Coverage Adsorbates for Heterogeneous Catalysis. *npj Comput Mater* 2020, *6* (1), 79. https://doi.org/10.1038/s41524-020-0345-2.
58. Shao, K.; Lele, A. D.; Shi, Z.; Von Miller, V.; Ju, Y.; Mesbah, A. Interpretable Attention-Based Transfer Learning in Plasma Catalysis: A Study on the Role of Surface Charge. *EES Catal.* 2025, *3*, 488–504. https://doi.org/10.1039/d4ey00256c.
59. Pillai, H. S.; Li, Y.; Wang, S.-H.; Omidvar, N.; Mu, Q.; Achenie, L. E. K.; Abild-Pedersen, F.; Yang, J.; Wu, G.; Xin, H. Interpretable Design of Ir-Free Trimetallic Electrocatalysts for Ammonia Oxidation with Graph Neural Networks. *Nat Commun* 2023, *14* (1), 792. https://doi.org/10.1038/s41467-023-36322-5.
60. Liang, C.; Rouzhahong, Y.; Ye, C.; Li, C.; Wang, B.; Li, H. Material Symmetry Recognition and Property Prediction Accomplished by Crystal Capsule Representation. *Nat Commun* 2023, *14* (1), 5198. https://doi.org/10.1038/s41467-023-40756-2.
61. Gu, G. H.; Noh, J.; Kim, S.; Back, S.; Ulissi, Z.; Jung, Y. Practical Deep-Learning Representation for Fast Heterogeneous Catalyst Screening. *J. Phys. Chem. Lett.* 2020, *11* (9), 3185–3191. https://doi.org/10.1021/acs.jpclett.0c00634.
62. Fung, V.; Hu, G.; Ganesh, P.; Sumpter, B. G. Machine Learned Features from Density of States for Accurate Adsorption Energy Prediction. *Nat Commun* 2021, *12* (1), 88. https://doi.org/10.1038/s41467-020-20342-6.
63. Studt, F.; Sharafutdinov, I.; Abild-Pedersen, F.; Elkjær, C. F.; Hummelshøj, J. S.; Dahl, S.; Chorkendorff, I.; Nørskov, J. K. Discovery of a Ni-Ga Catalyst for Carbon Dioxide Reduction to Methanol. *Nature Chem* 2014, *6* (4), 320–324. https://doi.org/10.1038/nchem.1873.
64. Sharafutdinov, I.; Elkjær, C. F.; Pereira De Carvalho, H. W.; Gardini, D.; Chiarello, G. L.; Damsgaard, C. D.; Wagner, J. B.; Grunwaldt, J.-D.; Dahl, S.; Chorkendorff, I. Intermetallic Compounds of Ni and Ga as Catalysts for the Synthesis of Methanol. *Journal of Catalysis* 2014, *320*, 77–88. https://doi.org/10.1016/j.jcat.2014.09.025.
65. Goyal, R.; Lee, W. J.; Sameer, S.; Sarkar, B.; Chiang, K.; Bordoloi, A. CNx Stabilized Ni-Ga Nanoparticles for CO2 Hydrogenation: Role of Preparation Methods. *Catalysis Today* 2020, *343*, 48–55. https://doi.org/10.1016/j.cattod.2019.03.031.
66. Mamun, O.; Winther, K. T.; Boes, J. R.; Bligaard, T. High-Throughput Calculations of Catalytic Properties of Bimetallic Alloy Surfaces. *Sci Data* 2019, *6* (1), 76. https://doi.org/10.1038/s41597-019-0080-z.

67. Dorogush, A. V.; Ershov, V.; Gulin, A. CatBoost: Gradient Boosting with Categorical Features Support. arXiv 2018. https://doi.org/10.48550/ARXIV.1810.11363.
68. Chen, T.; Guestrin, C. XGBoost: A Scalable Tree Boosting System. In *Proceedings of the 22nd ACM SIGKDD International Conference on Knowledge Discovery and Data Mining*; ACM: San Francisco California USA, 2016; pp 785–794. https://doi.org/10.1145/2939672.2939785.
69. Usuga, A. F.; Praveen, C. S.; Comas-Vives, A. Local Descriptors-Based Machine Learning Model Refined by Cluster Analysis for Accurately Predicting Adsorption Energies on Bimetallic Alloys. *J. Mater. Chem. A* 2024, *12* (5), 2708–2721. https://doi.org/10.1039/d3ta06316j.
70. Zimmerli, N.; Usuga, A.-F.; Checchia, S.; Comas Vives, A.; Müller, C.; Abdala, P. How Does the Ni-Ga Alloy Structure Tune Methanol Productivity and Selectivity? *ACS Catal*. 2025, *15*, 14252–14266. https://doi.org/10.1021/acscatal.5c02008.
71. Hjorth Larsen, A.; Jørgen Mortensen, J.; Blomqvist, J.; Castelli, I. E.; Christensen, R.; Dułak, M.; Friis, J.; Groves, M. N.; Hammer, B.; Hargus, C.; Hermes, E. D.; Jennings, P. C.; Bjerre Jensen, P.; Kermode, J.; Kitchin, J. R.; Leonhard Kolsbjerg, E.; Kubal, J.; Kaasbjerg, K.; Lysgaard, S.; Bergmann Maronsson, J.; Maxson, T.; Olsen, T.; Pastewka, L.; Peterson, A.; Rostgaard, C.; Schiøtz, J.; Schütt, O.; Strange, M.; Thygesen, K. S.; Vegge, T.; Vilhelmsen, L.; Walter, M.; Zeng, Z.; Jacobsen, K. W. The Atomic Simulation Environment—a Python Library for Working with Atoms. *J. Phys.: Condens. Matter* 2017, *29* (27), 273002. https://doi.org/10.1088/1361-648x/aa680e.
72. Paszke, A.; Gross, S.; Massa, F.; Lerer, A.; Bradbury, J.; Chanan, G.; Killeen, T.; Lin, Z.; Gimelshein, N.; Antiga, L.; Desmaison, A.; Köpf, A.; Yang, E.; DeVito, Z.; Raison, M.; Tejani, A.; Chilamkurthy, S.; Steiner, B.; Fang, L.; Bai, J.; Chintala, S. PyTorch: An Imperative Style, High-Performance Deep Learning Library. In *Proceedings of the 33rd International Conference on Neural Information Processing Systems*; Curran Associates Inc.: Red Hook, NY, USA, 2019.
73. Fey, M.; Lenssen, J. E. Fast Graph Representation Learning with PyTorch Geometric. arXiv 2019. https://doi.org/10.48550/ARXIV.1903.02428.
74. Kipf, T. N.; Welling, M. Semi-Supervised Classification with Graph Convolutional Networks. arXiv 2016. https://doi.org/10.48550/ARXIV.1609.02907.
75. Hamilton, W. L.; Ying, R.; Leskovec, J. Inductive Representation Learning on Large Graphs. arXiv 2017. https://doi.org/10.48550/ARXIV.1706.02216.
76. Morris, C.; Ritzert, M.; Fey, M.; Hamilton, W. L.; Lenssen, J. E.; Rattan, G.; Grohe, M. Weisfeiler and Leman Go Neural: Higher-Order Graph Neural Networks. arXiv 2018. https://doi.org/10.48550/ARXIV.1810.02244.
77. Veličković, P.; Cucurull, G.; Casanova, A.; Romero, A.; Liò, P.; Bengio, Y. Graph Attention Networks. arXiv 2017. https://doi.org/10.48550/ARXIV.1710.10903.

78. McInnes, L.; Healy, J.; Melville, J. UMAP: Uniform Manifold Approximation and Projection for Dimension Reduction. arXiv September 18, 2020. https://doi.org/10.48550/arXiv.1802.03426.
79. Giannozzi, P.; Andreussi, O.; Brumme, T.; Bunau, O.; Nardelli, M. B.; Calandra, M.; Car, R.; Cavazzoni, C.; Ceresoli, D.; Cococcioni, M.; Colonna, N.; Carnimeo, I.; Corso, A. D.; Gironcoli, S. de; Delugas, P.; Jr, R. A. D.; Ferretti, A.; Floris, A.; Fratesi, G.; Fugallo, G.; Gebauer, R.; Gerstmann, U.; Giustino, F.; Gorni, T.; Jia, J.; Kawamura, M.; Ko, H.-Y.; Kokalj, A.; Küçükbenli, E.; Lazzeri, M.; Marsili, M.; Marzari, N.; Mauri, F.; Nguyen, N. L.; Nguyen, H.-V.; Otero-de-la-Roza, A.; Paulatto, L.; Poncé, S.; Rocca, D.; Sabatini, R.; Santra, B.; Schlipf, M.; Seitsonen, A. P.; Smogunov, A.; Timrov, I.; Thonhauser, T.; Umari, P.; Vast, N.; Wu, X.; Baroni, S. Advanced Capabilities for Materials Modelling with QUANTUM ESPRESSO. *Journal of Physics: Condensed Matter* 2017, *29* (46), 465901.
80. Giannozzi, P.; Baroni, S.; Bonini, N.; Calandra, M.; Car, R.; Cavazzoni, C.; Ceresoli, D.; Chiarotti, G. L.; Cococcioni, M.; Dabo, I.; Dal Corso, A.; De Gironcoli, S.; Fabris, S.; Fratesi, G.; Gebauer, R.; Gerstmann, U.; Gougoussis, C.; Kokalj, A.; Lazzeri, M.; Martin-Samos, L.; Marzari, N.; Mauri, F.; Mazzarello, R.; Paolini, S.; Pasquarello, A.; Paulatto, L.; Sbraccia, C.; Scandolo, S.; Sclauzero, G.; Seitsonen, A. P.; Smogunov, A.; Umari, P.; Wentzcovitch, R. M. QUANTUM ESPRESSO: A Modular and Open-Source Software Project for Quantum Simulations of Materials. *J. Phys.: Condens. Matter* 2009, *21* (39), 395502. https://doi.org/10.1088/0953-8984/21/39/395502.
81. Wellendorff, J.; Lundgaard, K. T.; Møgelhøj, A.; Petzold, V.; Landis, D. D.; Nørskov, J. K.; Bligaard, T.; Jacobsen, K. W. Density Functionals for Surface Science: Exchange-Correlation Model Development with Bayesian Error Estimation. *Phys. Rev. B* 2012, *85* (23), 235149. https://doi.org/10.1103/PhysRevB.85.235149.
82. Kresse, G.; Hafner, J. Ab Initio Molecular Dynamics for Liquid Metals. *Phys. Rev. B* 1993, *47* (1), 558–561. https://doi.org/10.1103/PhysRevB.47.558.
83. Kresse, G.; Furthmüller, J. Efficiency of Ab-Initio Total Energy Calculations for Metals and Semiconductors Using a Plane-Wave Basis Set. *Computational Materials Science* 1996, *6* (1), 15–50. https://doi.org/10.1016/0927-0256(96)00008-0.
84. Kresse, G.; Hafner, J. Ab Initio Molecular-Dynamics Simulation of the Liquid-Metal–Amorphous-Semiconductor Transition in Germanium. *Phys. Rev. B* 1994, *49* (20), 14251–14269. https://doi.org/10.1103/PhysRevB.49.14251.
85. Pedregosa, F.; Varoquaux, G.; Gramfort, A.; Michel, V.; Thirion, B.; Grisel, O.; Blondel, M.; Prettenhofer, P.; Weiss, R.; Dubourg, V.; Vanderplas, J.; Passos, A.; Cournapeau, D.; Brucher, M.; Perrot, M.; Duchesnay, É. Scikit-Learn: Machine Learning in Python. *J. Mach. Learn. Res.* 2011, *12*, 2825–2830.

Figures

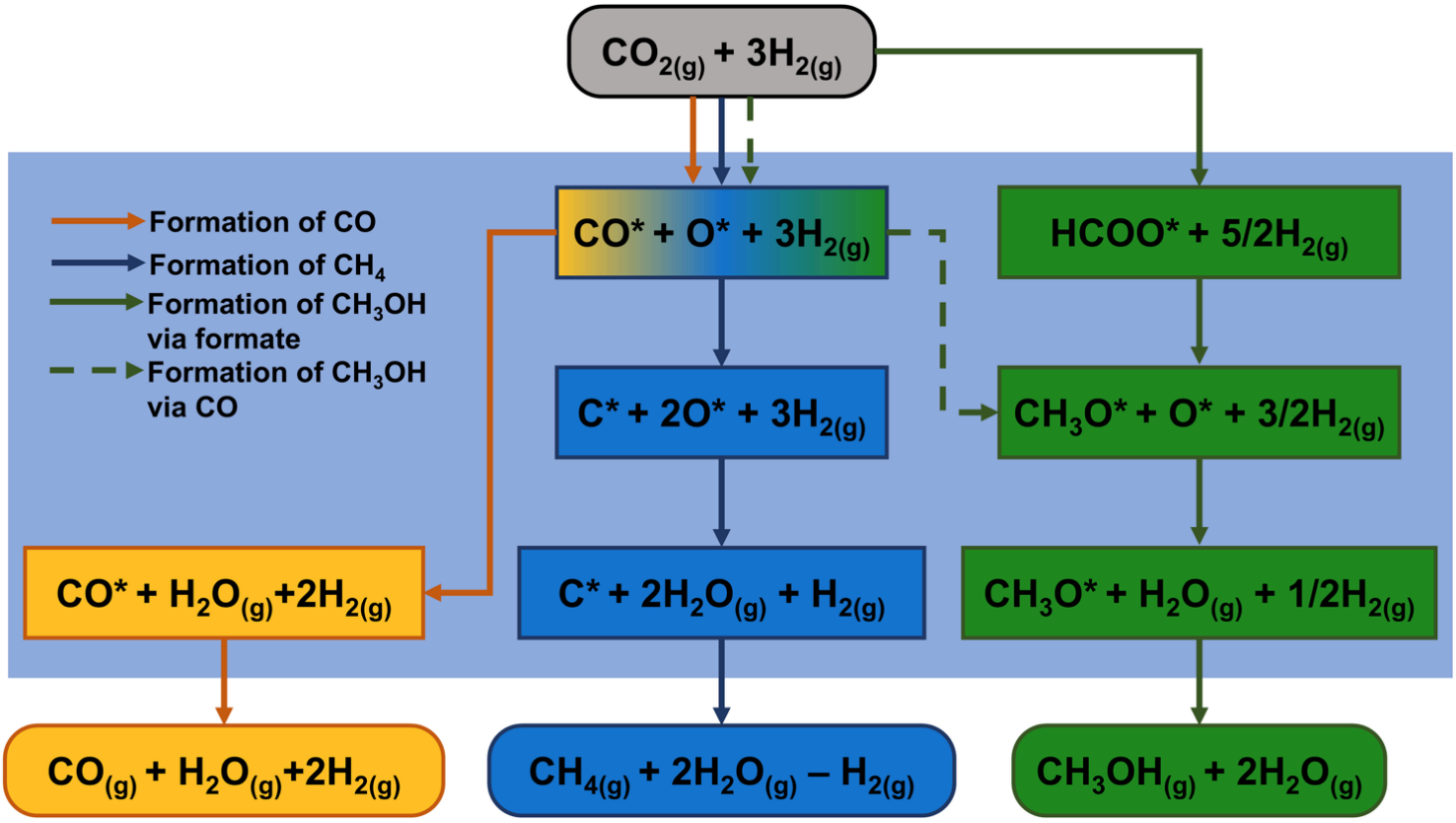


Figure 1

Reaction scheme for CO_2 hydrogenation to methanol, including the formation pathways of $CO_{(g)}$, $CH_{4(g)}$, and $CH_3OH_{(g)}$. Oval nodes involve gas-phase species that are not included in the dataset. Square box nodes indicate that at least one key intermediate is adsorbed on a surface model; all these reaction steps are included.

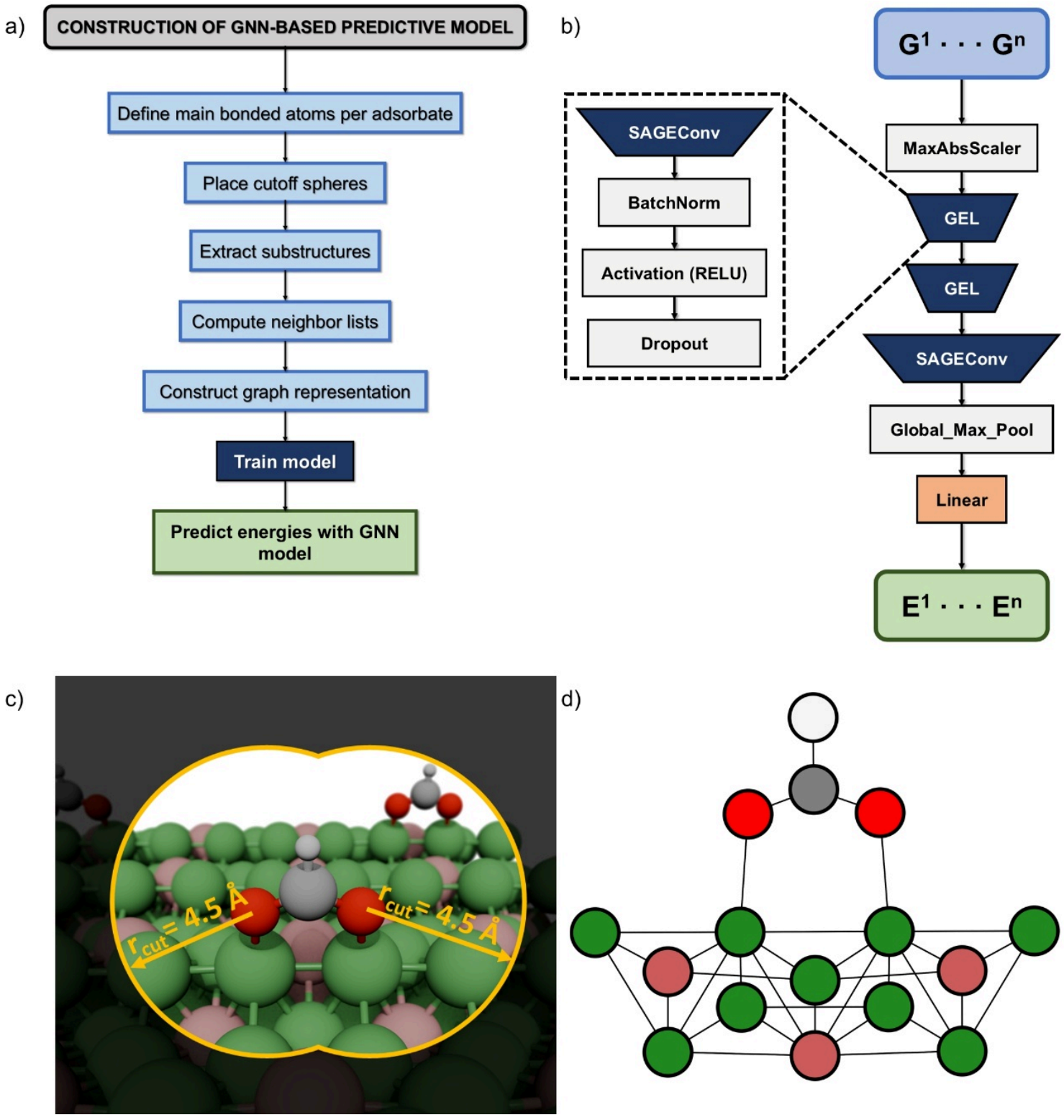


Figure 2

a) Schematic workflow for constructing the GNN-based predictive model. b) Architecture of the GNN-based model. c) Centered on cutoff spheres on main bonded atoms in the adsorbates (HCOO*). d) Graph representation of substructure for the local adsorption site obtained from the cutoff spheres (HCOO*), green atoms represent Ni, salmon atoms represent Ga, red atoms represent O, grey atoms represent C, white atoms represent H.

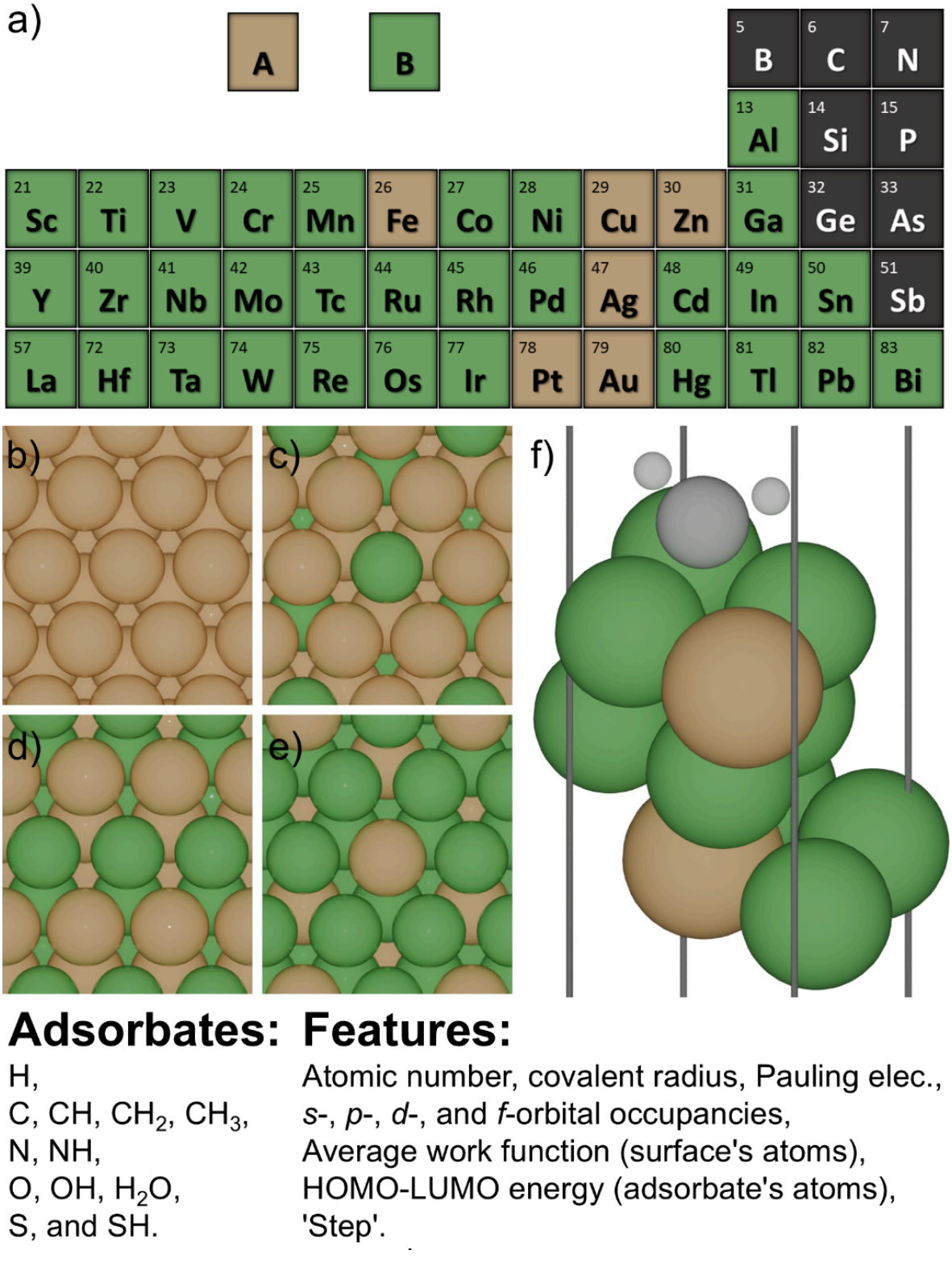


Figure 3

a) List of metals constituting the A_nB_m bimetallic alloy, yellow corresponds to A, while the blue ones to B. Top view of different Cu-based alloys: b) Cu_{12}, c) Cu_9Ni_3, d) Cu_6Ni_6, and e) Cu_3Ni_9, representing different stoichiometric combinations of A=Cu and B=Ni used in the

alloy's dataset. f) Side view of slab model for Cu_3Ni_9 with CH_2 adsorbed on hollow position. Brown atoms represent Cu; green atoms represent Ni.

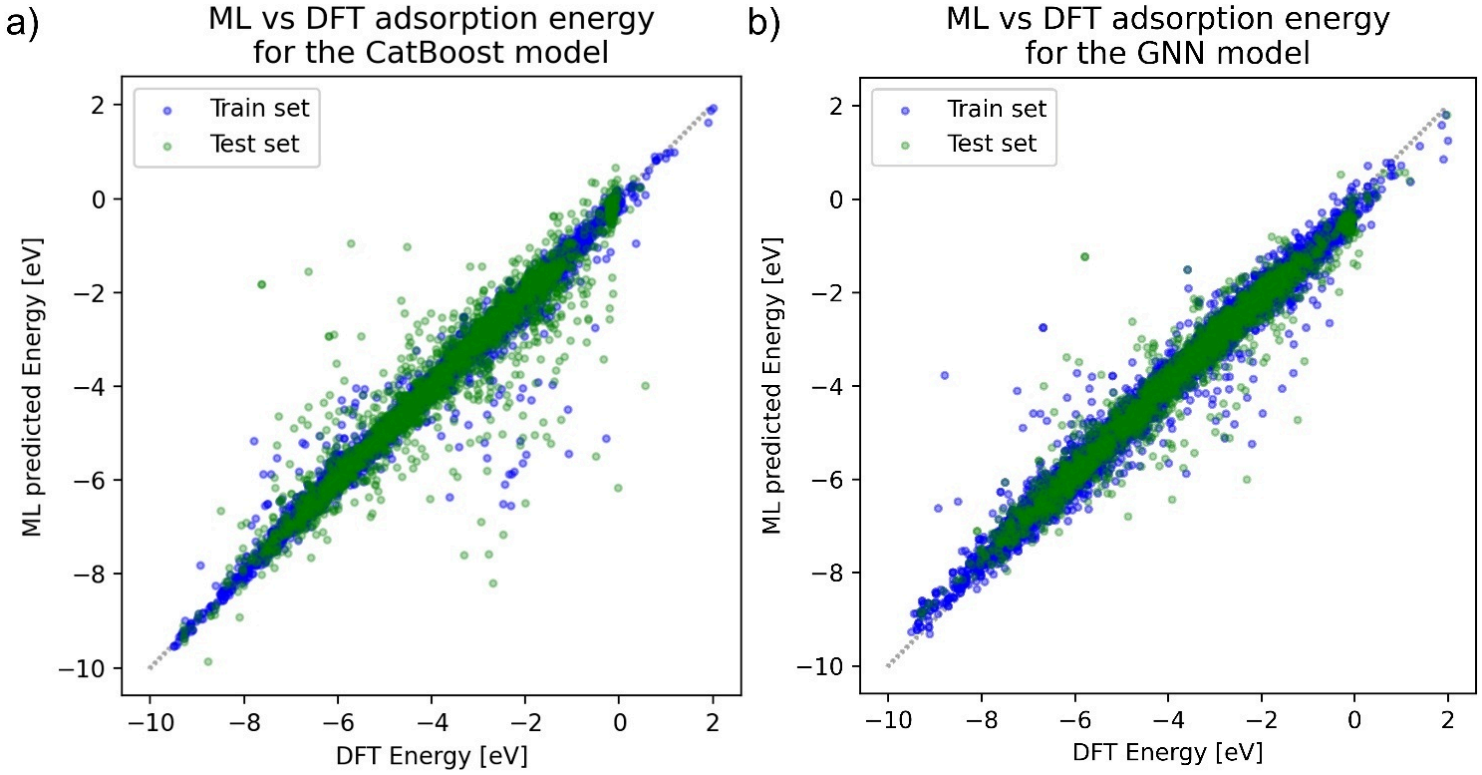


Figure 4

Parity plot of DFT-calculated vs ML-predicted adsorption energies for a) the CatBoost model and b) the GNN-based model.

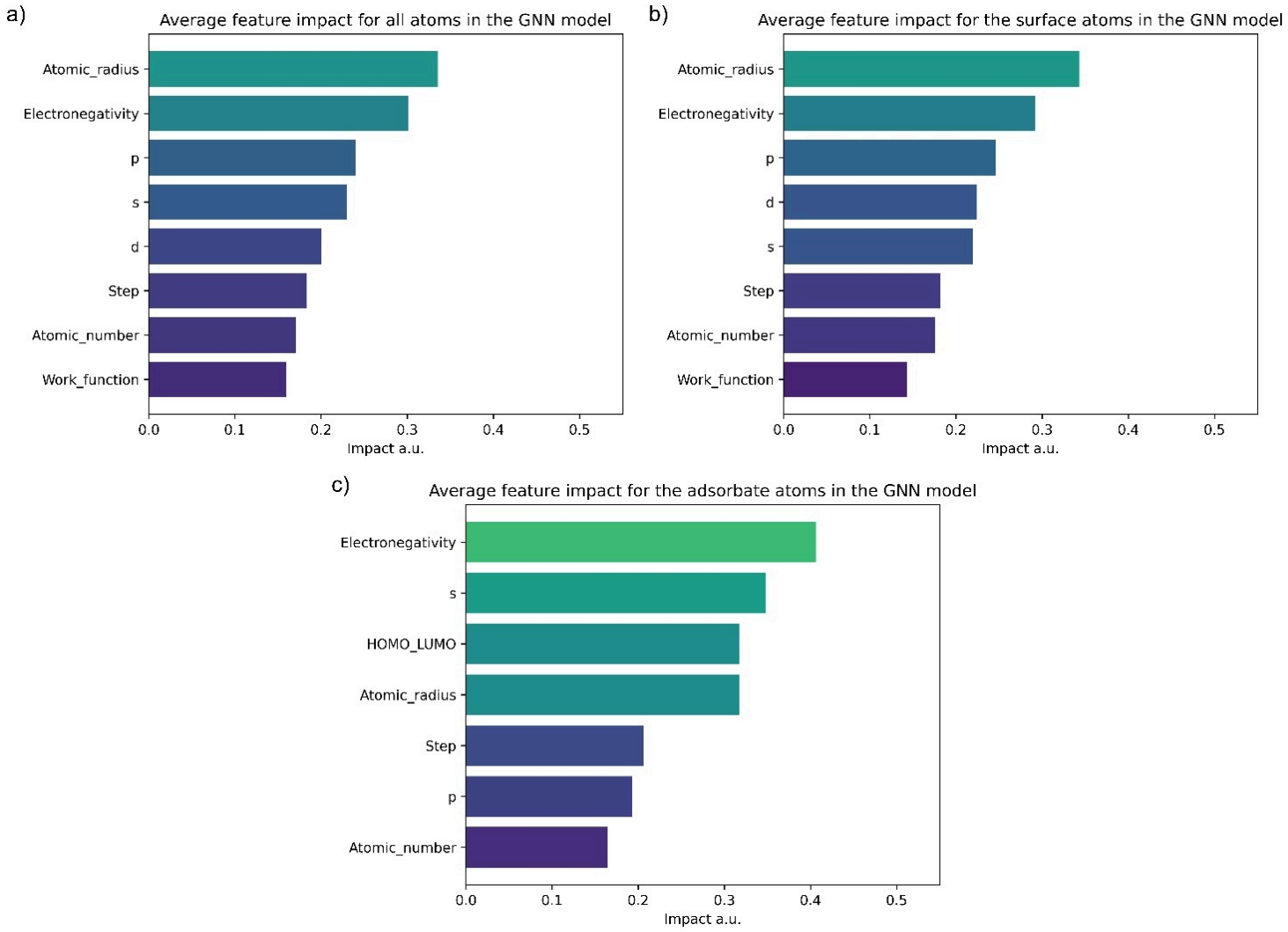


Figure 5

Average feature importance for the GNN model on the alloy's dataset using the training set for: a) all atoms, b) surface atoms, and c) adsorbate atoms. The term 'work function', as presented on the average impact across all atoms, represents the combined average contribution of both the surface work function and the HOMO-LUMO energy of the adsorbates.

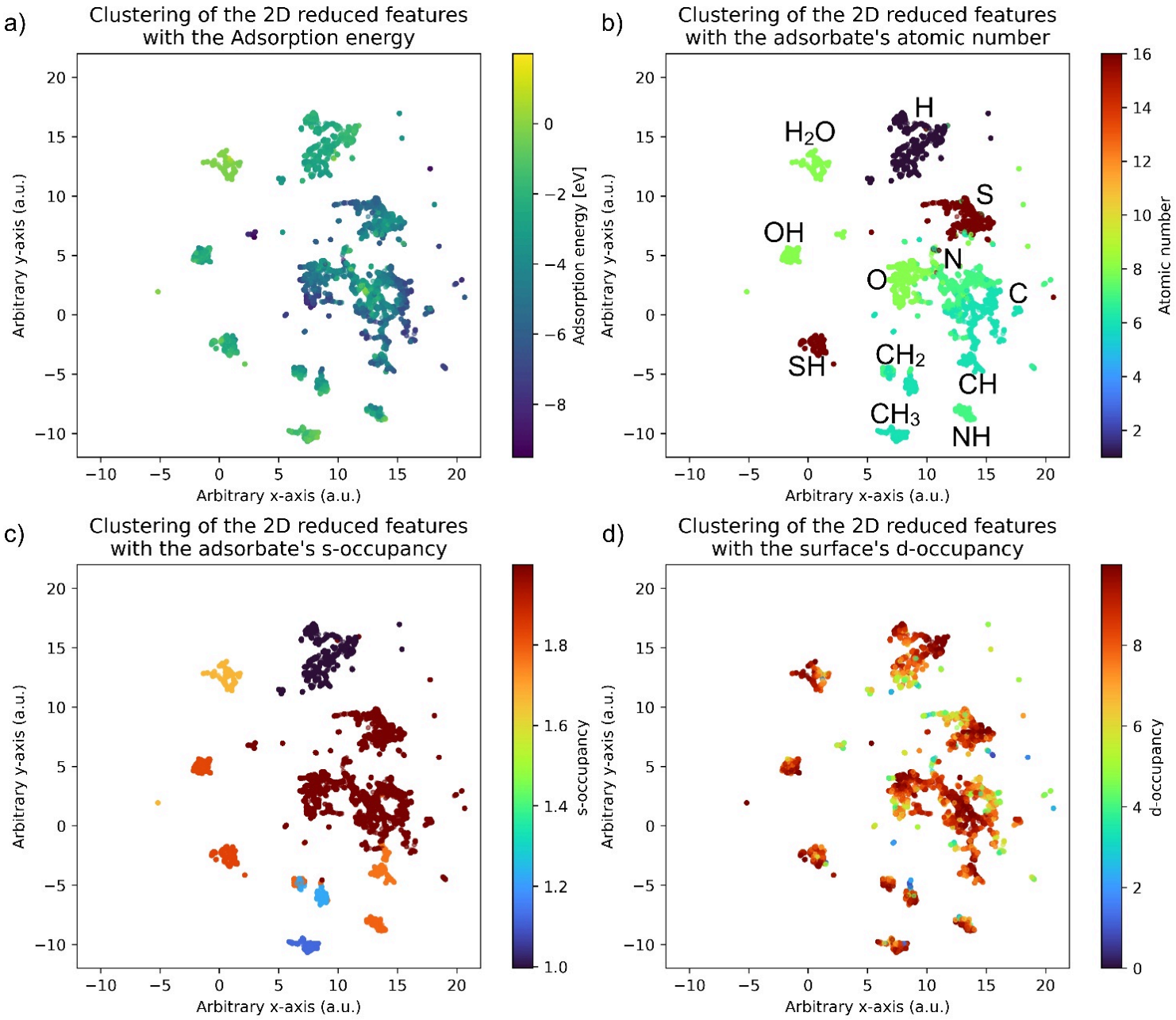


Figure 6

UMAP-based 2D dimensionality reduction of pooled graph embeddings on the training set. Visualization of 2D reduced dimension with a) the adsorption energy, b) atomic number, c) *s*-orbital occupancy of the main adsorbate bonding atom on the surface, and d) average *d*-orbital occupancy of surface atoms.

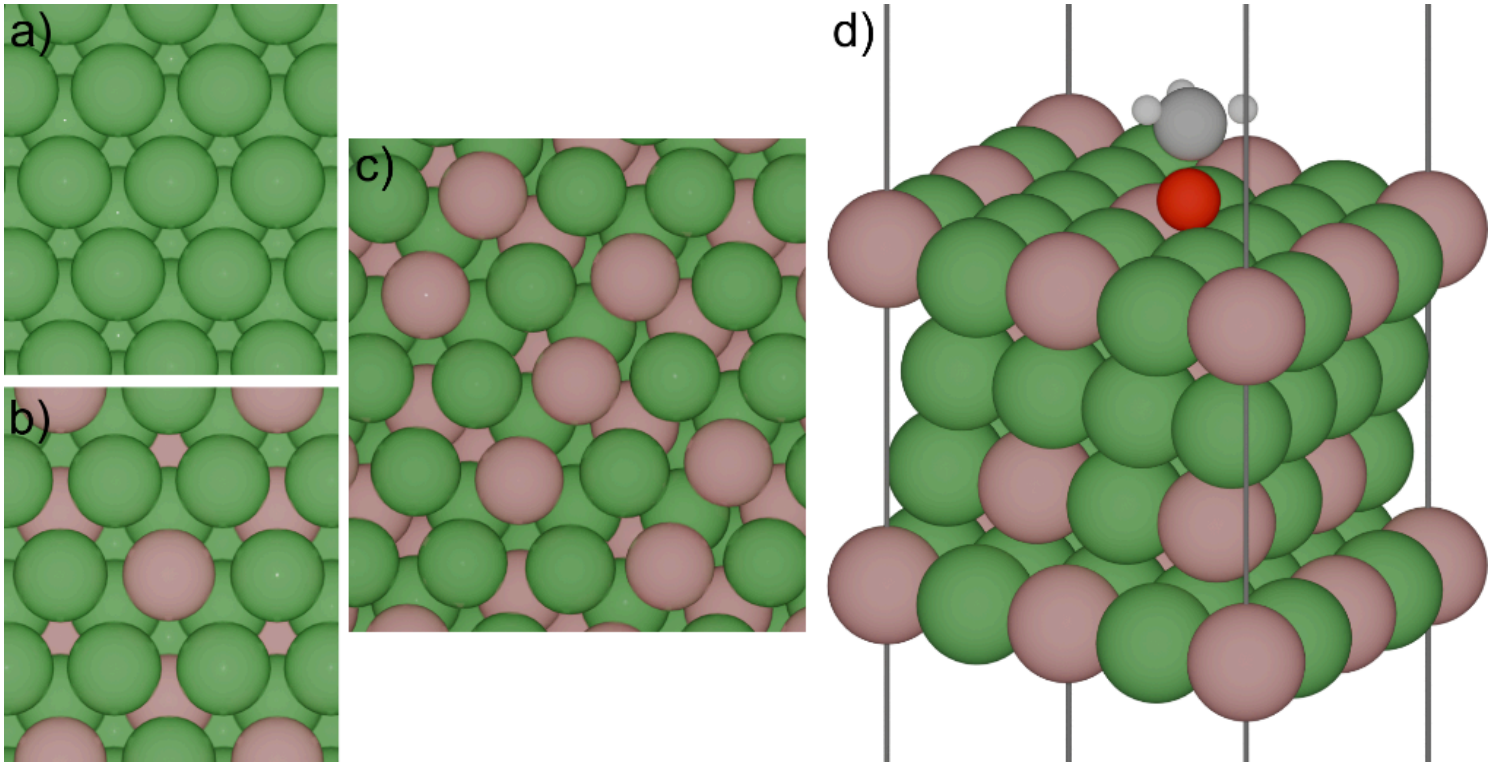


Figure 7

Top view of: a) Ni, b) Ni_3Ga, and c) Ni_5Ga_3, representing flat surface models used in the Ni-Ga dataset. d) Side view of slab model for $Ni_5Ga_3(221)$ with CH_3O* adsorbed on hollow position.

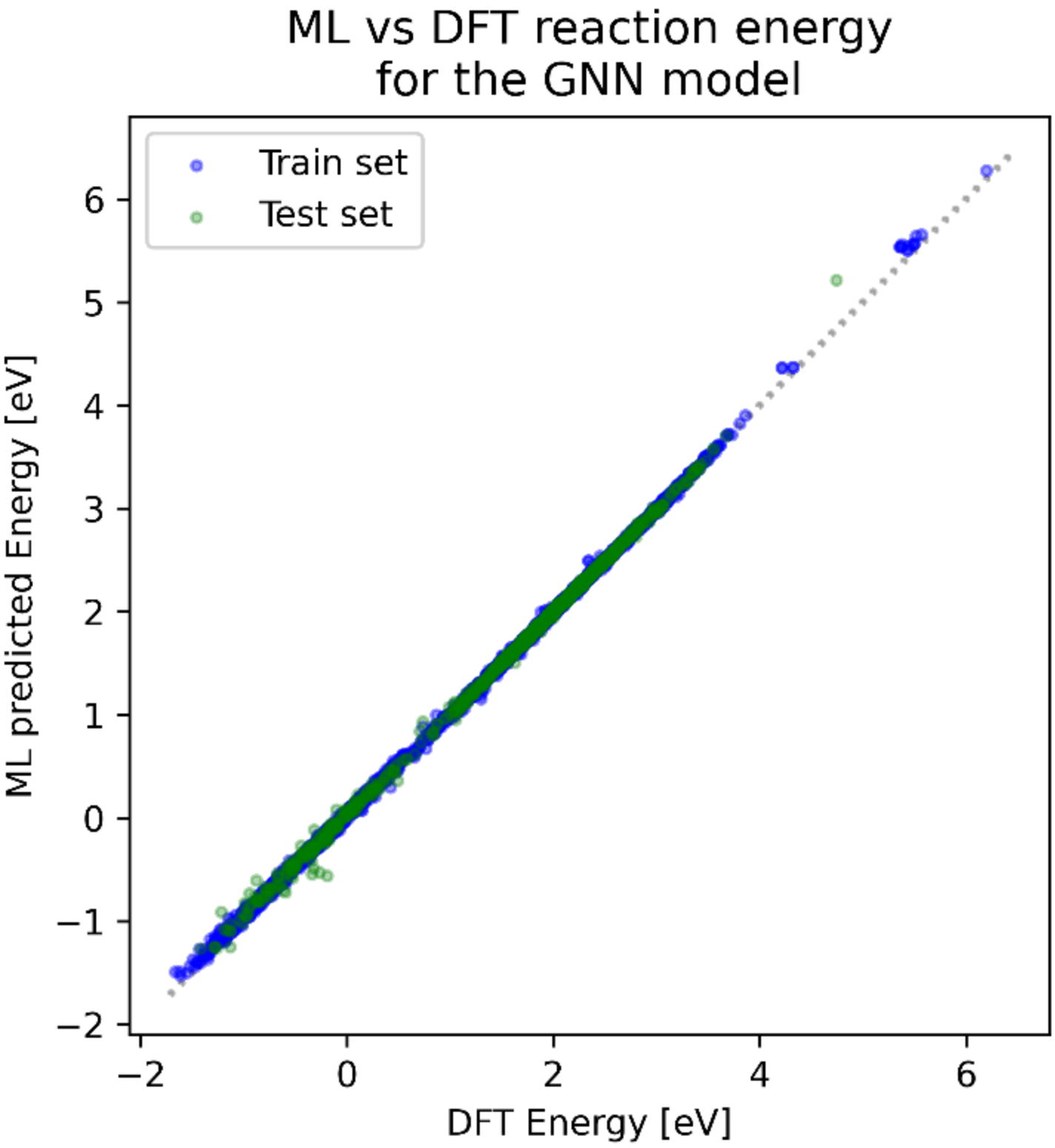


Figure 8

Parity plot of DFT-calculated vs ML-predicted reaction energies for the GNN-based Model.

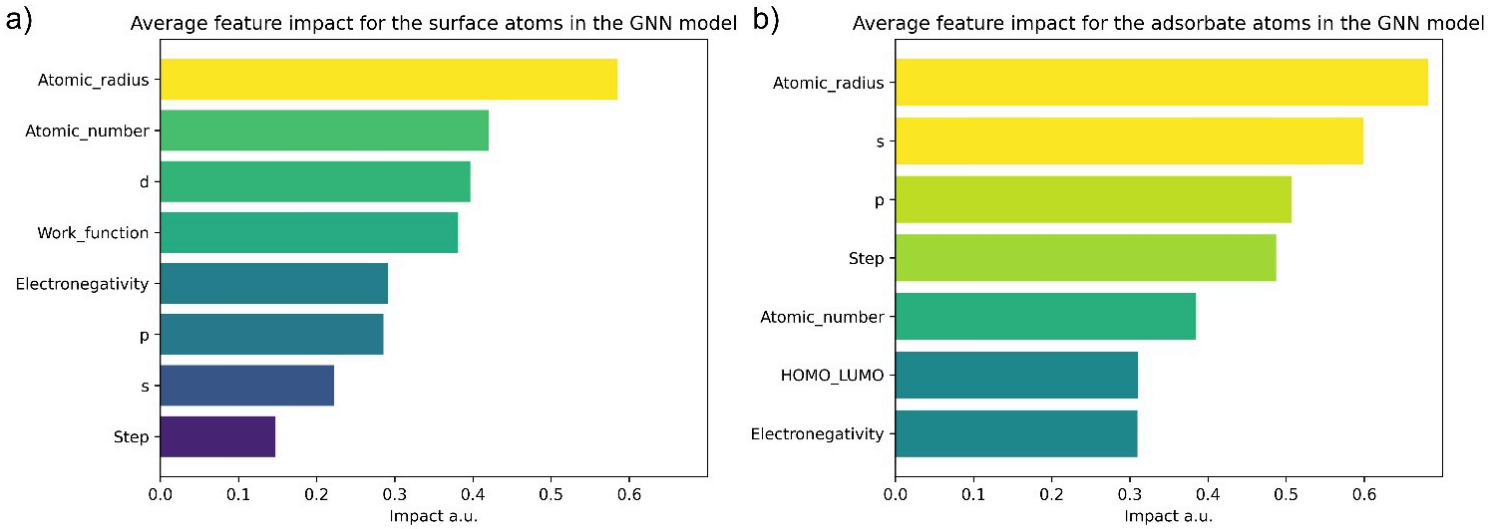


Figure 9

Average feature importance for the GNN model on the Ni-Ga dataset using the training set for: a) surface atoms, and b) adsorbate atoms.

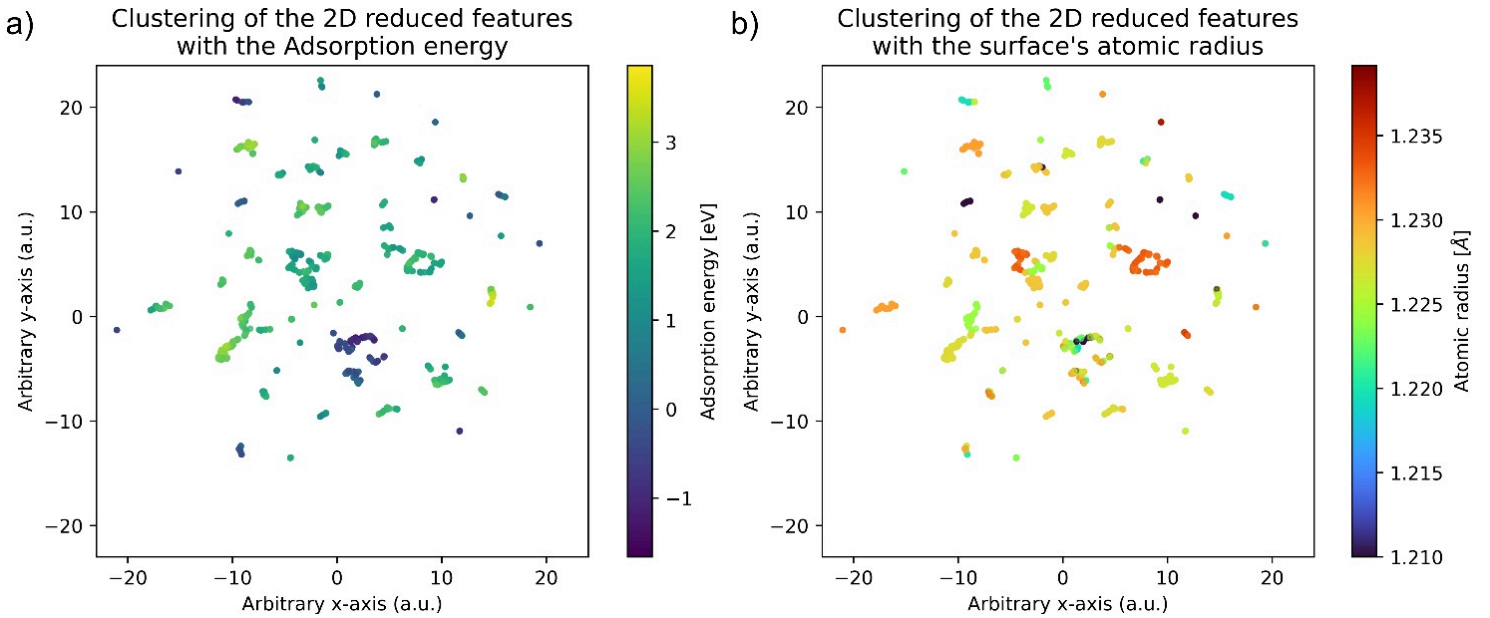


Figure 10

UMAP-based 2D dimensionality reduction of pooled graph embeddings on the training set. Visualization of 2D reduced dimension with a) the reaction energy, and b) the atomic radius of surface atoms. The range of energy is plotted from -2 to 4 eV.

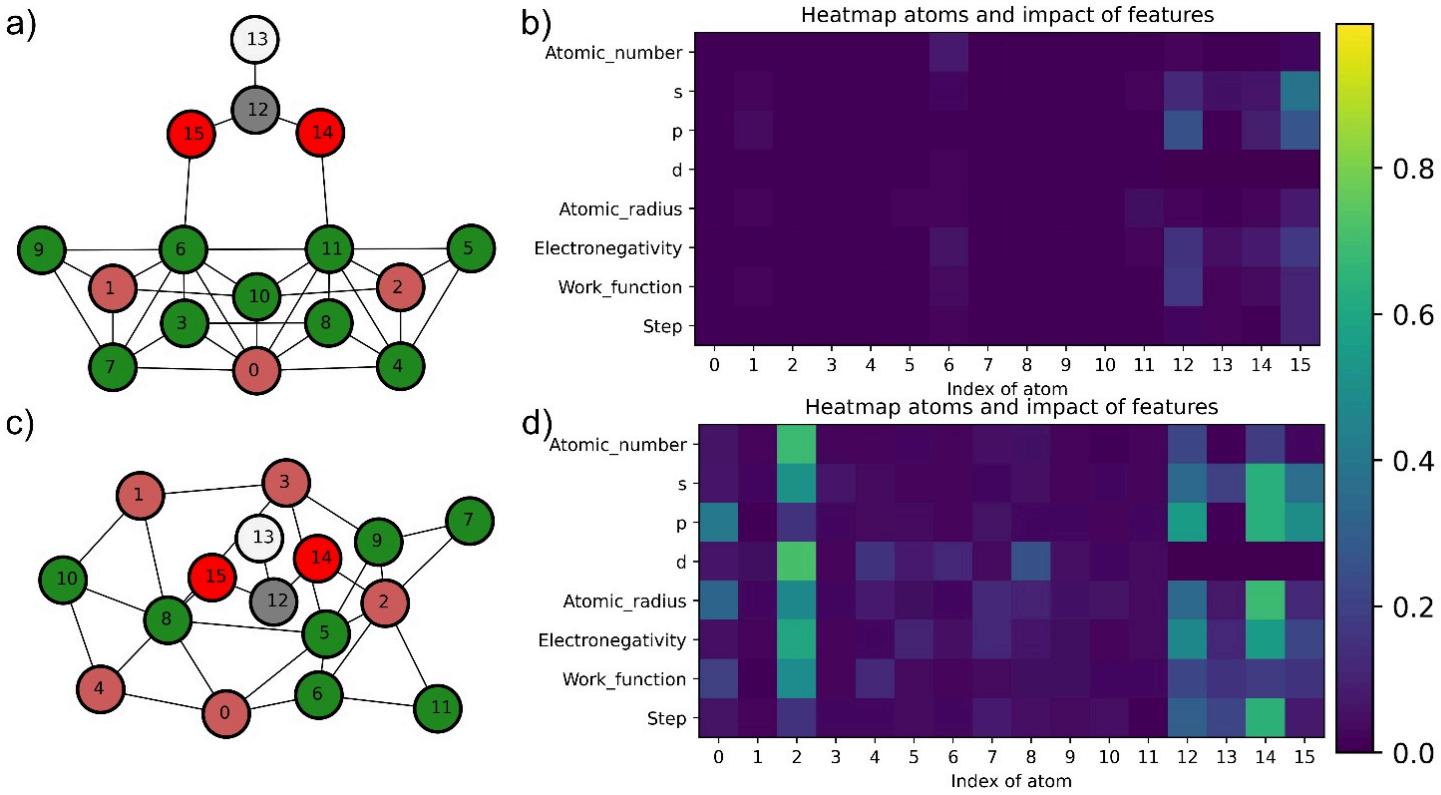


Figure 11

Graph representation and their corresponding heatmaps showing the impact of features per atom for: (a-b) the most stable HCOO* substructure, which has the lowest reaction energy; and (c-d) the least stable HCOO* substructure, along with its corresponding graph and heatmap. The index numbers in the substructure correspond to the index of atoms in the heatmap plot. The term 'work function' represents the surface work function (Index 0 - 11) and the HOMO-LUMO energy of the adsorbates (Index 12 - 15) for both substructures.

Supplementary Files

This is a list of supplementary files associated with this preprint. Click to download.

- GNN2ESInpjcomputmat040925.docx